Theory of supercompression of vapor bubbles and nanoscale thermonuclear fusion

Robert I. Nigmatulin,[a] Iskander Sh. Akhatov,[b] Andrey S. Topolnikov, Raisa Kh. Bolotnova, and Nailya K. Vakhitova
Institute of Mechanics, Ufa Branch of the Russian Academy of Sciences, 6 Karl Marx Street, Ufa 450000, Russia

Richard T. Lahey, Jr.
Department of Mechanical, Aerospace, and Nuclear Engineering, Rensselaer Polytechnic Institute, 110 8th Street, Troy, New York 12180-3590

Rusi P. Taleyarkhan
School of Nuclear Engineering, Purdue University, West Lafayette, Indiana 47907-1290

(Received 10 November 2004; accepted 12 September 2005; published online 25 October 2005)

This paper provides the theoretical basis for energetic vapor bubble implosions induced by a standing acoustic wave. Its primary goal is to describe, explain, and demonstrate the plausibility of the experimental observations by Taleyarkhan *et al.* [Science **295**, 1868 (2002); Phys. Rev. E **69**, 036109 (2004)] of thermonuclear fusion for imploding cavitation bubbles in chilled deuterated acetone. A detailed description and analysis of these data, including a resolution of the criticisms that have been raised, together with some preliminary HYDRO code simulations, has been given by Nigmatulin *et al.* [Vestnik ANRB (Ufa, Russia) **4**, 3 (2002); J. Power Energy **218-A**, 345 (2004)] and Lahey *et al.* [Adv. Heat Transfer (to be published)]. In this paper a hydrodynamic shock (i.e., HYDRO) code model of the spherically symmetric motion for a vapor bubble in an acoustically forced liquid is presented. This model describes cavitation bubble cluster growth during the expansion period, followed by a violent implosion during the compression period of the acoustic cycle. There are two stages of the bubble dynamics process. The first, low Mach number stage, comprises almost all the time of the acoustic cycle. During this stage, the radial velocities are much less than the sound speeds in the vapor and liquid, the vapor pressure is very close to uniform, and the liquid is practically incompressible. This process is characterized by the inertia of the liquid, heat conduction, and the evaporation or condensation of the vapor. The second, very short, high Mach number stage is when the radial velocities are the same order, or higher, than the sound speeds in the vapor and liquid. In this stage high temperatures, pressures, and densities of the vapor and liquid take place. The model presented herein has realistic equations of state for the compressible liquid and vapor phases, and accounts for nonequilibrium evaporation/condensation kinetics at the liquid/vapor interface. There are interacting shock waves in both phases, which converge toward and reflect from the center of the bubble, causing dissociation, ionization, and other related plasma physics phenomena during the final stage of bubble collapse. For a vapor bubble in a deuterated organic liquid (e.g., acetone), during the final stage of collapse there is a nanoscale region (diameter $\sim$100 nm) near the center of the bubble in which, for a fraction of a picosecond, the temperatures and densities are extremely high ($\sim 10^8$ K and $\sim$10 g/cm^3, respectively) such that thermonuclear fusion may take place. To quantify this, the kinetics of the local deuterium/deuterium (D/D) nuclear fusion reactions was used in the HYDRO code to determine the intensity of the fusion reactions. Numerical HYDRO code simulations of the bubble implosion process have been carried out for the experimental conditions used by Taleyarkhan *et al.* [Science **295**, 1868 (2002); Phys. Rev. E **69**, 036109 (2004)] at Oak Ridge National Laboratory. The results show good agreement with the experimental data on bubble fusion that was measured in chilled deuterated acetone. © *2005 American Institute of Physics*. [DOI: 10.1063/1.2104556]

I. INTRODUCTION

This paper is concerned with the analysis of the so-called bubble fusion experiments which were performed by Taleyarkhan *et al.*[1,2] at Oak Ridge National Laboratory (ORNL). The publication of these results caused both excitement and controversy within the scientific community. The most significant criticisms raised were subsequently discussed and resolved by Nigmatulin, Taleyarkhan, and Lahey[3,4] and by Lahey *et al.*[5]

The intensive implosion of gas and/or vapor bubbles, including bubbles induced by acoustic cavitation, may lead to ultrastrong compressions and temperatures, and light

[a]Author to whom correspondence should be addressed. Telephone: +7-3472-73-7051. Fax: +7-3472-73-3569. Electronic mail: nigmar@anrb.ru
[b]Current address: Department of Mechanical Engineering and Applied Mechanics, North Dakota State University, Dolve Hall, Fargo, ND 58150.

pulses due to sonoluminescence.[5–20] Both multibubble sonoluminescence (MBSL) and single bubble sonoluminescence (SBSL) have been studied, and these interesting phenomena have been thoroughly reviewed by Margulis[19] and Young.[20]

It is not normally possible to measure the maximum temperatures during sonoluminescence experiments, where the emission spectrum is related to electron temperatures of more than 10^4 K, because the emitted photons are strongly absorbed by the highly compressed, optically thick gas in the bubble as well as in a thin liquid layer around it. Rather, one normally infers these temperatures from calculations. In particular, Moss *et al.*[21–23] presented the results of detailed HYDRO code simulations of the spherically symmetric dynamics of a noncondensable gas bubble in an acoustic field with a frequency of 20–40 kHz and amplitude of about 1 bar. Typical situations for single bubble sonoluminescence (SBSL) were considered, when a noncondensable bubble grew from a radius of 4.5 μm to about 44 μm during the acoustic expansion phase and then imploded to a radius of about 0.3 μm during the acoustic compression phase. In spite of some incorrect assumptions (see Ref. 24) the basic conclusions in Moss *et al.*'s papers are qualitatively correct for the final stage of the bubble implosion. During this stage, which lasted only about 10^{-3} μs (out of the $30-50$ μs acoustic driving period), a shock wave may be initiated from the interface and it accelerates and intensifies towards the bubble's center. This shock wave implodes (i.e., cumulates to), and reflects from, the center of the bubble, compressing and heating the gas there to very high pressures and temperatures. Also at this moment, a high-density ionized gas core is formed near the bubble's center. A range of peak temperatures have been calculated,[20–23] varying from 10^4 K to 10^6 K. According to Moss *et al.*'s calculations, the radius of this core region is 10^{-9} m, and during a time interval $10^{-11}-10^{-10}$ s, ions in the core attain a density of $\rho_{\max} \approx 10$ g/cm^3 and temperature of $T_{\max} \approx 10^6$ K, while the temperature of the electrons that define the light emission is only about one third of the ion temperature. Significantly, recent SBSL experiments (Camara, Putterman, and Kirilov[25]) using very small gas bubbles and high-frequency acoustic excitation also imply peak temperatures of 10^6 K.

The calculations of Moss *et al.*,[21,22] and those of Vuong and Szeri,[26] also yielded an important experimental confirmation; the time duration of the light pulse, defining the time duration of the supercompressed central core, was $\sim 10^{-10}$ s, and these predictions agreed well with the experimental measurements of Barber *et al.*[7] and Gompf *et al.*[27] for light emission durations during SBSL.

We note that the large temperatures in the highly compressed central gas core of the bubble are accomplished at the expense of the cumulative (i.e., focused) conversion into the gas' internal energy of a part of the kinetic energy of the liquid that is accelerated towards the bubble's center by the acoustic field. The higher the liquid's kinetic energy, the stronger the compression and heat-up of the central core region.

The goal of the bubble fusion (i.e., sonofusion) experiments at ORNL (Taleyarkhan *et al.*[1,2]) was to achieve a two orders of magnitude increase in peak temperature (i.e., to 10^8 K) compared to typical sonoluminescence experiments, thus creating conditions suitable for thermonuclear fusion. In order to achieve this, a *fundamental change* in experimental technique was made, which allowed one to increase many times the kinetic energy of the liquid accelerated toward the bubble's center, thus greatly enhancing the effect of cumulative shock wave compression. In particular:

(1) An order-of-magnitude higher amplitude of the standing acoustic field was used. Namely, instead of the traditional 1–1.5 bars used in SBSL experiments, more powerful acoustic fields with amplitudes of 15 bars or more[28] were applied. To achieve higher acoustic forcing one has to overcome several difficulties. First was to find a liquid, which could be put into significant tension (i.e., -15 bars) before cavitation, which was then nucleated at the proper moment of acoustical rarefaction using high-energy neutrons. Second, to create and focus such intensive acoustic fields within a small region of the liquid pool (i.e., at the center of the acoustic antinode).

(2) Unlike SBSL, where noncondensable gas bubbles are used, in the bubble fusion experiments of Taleyarkhan *et al.*[1,2] vapor cavitation bubbles were used. That is, the bubbles formed are filled with vapor of the surrounding liquid. In vapor bubbles the cushioning of the implosion due to the increasing pressure of the compressed vapor can be minimized. That is, as the vapor bubble implodes the vapor pressure stays essentially constant until the final stage of collapse due to vapor condensation at bubble's interface, and possibly, the homogeneous nucleation of droplets within the imploding bubble. This condensation (which ceases when thermodynamic critical conditions are achieved) greatly reduces cushioning of the vapor compression process and increases the peak pressure, density, and temperature.

(3) In the experiments of Taleyarkhan *et al.*[1,2] the bubbles, or more precisely the clusters of nucleation cavities, were created by fast neutrons at the moment of strongest liquid tension. These bubble nuclei had an initial radius, $a_0 = 10-100$ nm (Lahey *et al.*[5]). Because of the high liquid superheat (i.e., tension) that exists, these nuclei give rise to a rapidly growing cluster of vapor bubbles during the expansion stage, attaining a maximum radius of the bubbles of $a_{\max} = 300-800$ μm. These values were predicted by our calculations but not in the experiments.[1,2] In the experiments only the bubble cluster containing many bubbles was photographed using high speed video, and a maximum cluster radius of $R = 4$ mm was measured. Nevertheless, for realistic estimates on bubble packing, our predictions of maximum bubble radius seem reasonable. In any event, it should be noted that a bubble radius of $a_{\max} = 300-800$ μm is an order of magnitude more than in typical SBSL experiments ($a_{\max} \approx 50-80$ μm). Thus, in the ORNL experiments the maximum volume of each bubble was 10^3 times larger than in typical SBSL experiments and there was a cluster of about 10^3 bubbles. Moreover, because of the

above-mentioned reduced cushioning due to intentional degassing, and the higher compression by a more intensive acoustic field in the liquid around the bubble, the liquid is accelerated towards the bubble's center, attaining $\sim 10^4 - 10^5$ times larger kinetic energies than occur in typical SBSL experiments. This implies much higher compression, and thus higher density, pressure, and temperature near the bubble's center. The effect of maximum bubble size, $a_{\max}$, and the radial speed of bubble implosion, w, on the intensification of gas compression were confirmed experimentally by Delgadino, Bonetto, and Lahey[17] and by Moraga *et al.*,[18] respectively. In these SBSL experiments, as a result of moderate increases in $a_{\max}$ ($\sim 50\%$), or increases in the speed of the interface during implosion, w, it was possible to achieve a substantial enhancement in light emission during the implosions.

(4) The test liquid used in Taleyarkhan *et al.*[1,2] experiments was a well-degassed organic liquid. In particular, acetone of two isotopic compositions; normal acetone (C_3H_6O, denoted herein as H-acetone) was the control liquid, and deuterated acetone (C_3D_6O, D-acetone) was the test liquid. Each molecule of D-acetone contains six deuterium nuclei, which may undergo thermonuclear fusion reaction at high enough temperatures and densities. Acetone also possesses high cavitation stability; that is, it can withstand high-tension states in liquid without premature cavitation. Moreover, organic liquids, such as acetone, also have relatively high accommodation (i.e., condensation/evaporation) coefficients, which, together with a sufficiently low liquid pool temperature, promote a lower evaporation rate during bubble expansion and more intensive vapor condensation during bubble implosion. In addition, due to a relatively high molecular weight, M ($M=64$ for D-acetone), and low adiabatic exponent ($\gamma=1.125$ for acetone vapor), organic vapor has a relatively low speed of sound ($C_G=\sqrt{(\gamma \mathrm{R}/M)T}$, $\mathrm{R}=8314$ J/(kmol K) is the universal gas constant), which, for fixed liquid interfacial implosion speeds, leads to the formation of stronger shock waves than in some other gases and vapors of potential interest. In addition, a low γ leads to high maximum compression in the shock wave within the bubble, $\sim(\gamma+1)/(\gamma-1)$.

The importance of vapor trapping on SBSL has been previously discussed by Colussi, Weavers, and Hoffman[29] and by Storey and Szeri,[30] and the effect of molecular mass on sound speed was considered in SBSL by Vuong and Szeri.[26]

Didenko and Suslick[31] have raised some concerns about energy conversion efficiency during bubble implosions since endothermic chemical reactions (associated with the dissociation processes) and radiation losses may utilize liquid kinetic energy that would otherwise be converted to the gas/vapor's internal energy during typical SBSL and MBSL sonochemistry experiments. However, in bubble fusion experiments the time scale during the final phase of the implosion process is much shorter (10^{-13} s) than in typical SBSL (10^{-10} s) and MBSL sonochemistry experiments (10^{-9} s), and thus the time for absorption of energy by the electrons and the resultant radiation energy losses are insufficient to have much effect on energy conversion efficiency. In contrast, the energy losses due to dissociation and ionization are crucial in MBSL experiments, where the maximum temperature is $\sim 10^4$ K and in SBSL experiments, where the maximum temperature is about $10^5 - 10^6$ K, but they are not crucial for bubble fusion experiments since the maximum temperature is at least 10^8 K. As discussed in Sec. IV D, the energy required for dissociation and ionization is $\sim 0.1 - 1.0$ keV $\approx 10^6 - 10^7$ K, thus compared with bubble fusion temperatures, $>10^8$ K, the effective temperature reduction is less than 5% (see Fig. 14 later in this article). Anyway, as discussed in Sec. XI, all these losses were simulated carefully because they have an influence on shock wave transformations before the final focusing, and at lower temperatures well before the initiation of D/D fusion. Also, evaporation and condensation have an influence on the process although they occur at even lower temperatures and involve less energy transfers than do dissociation and ionization.

In this paper we present a mathematical model that describes, explains, and demonstrates the plausibility of the experimental observations at ORNL of thermonuclear fusion for an imploding cavitation bubble in chilled deuterated acetone (Taleyarkhan *et al.*[1,2]). For the reader's convenience, in Sec. II we briefly describe the experimental setup at ORNL and some of the key results. Section III contains a discussion of the main assumptions and approximations in the theoretical model. Realistic equations of state for acetone are proposed in Sec. IV. The full set of equations describing the low Mach number phase of the bubble dynamic process is given in Sec. V. Condensation and evaporation kinetics are given in Sec. VI. Section VII is devoted to the high Mach number phase of the bubble implosion process with emphasis on the highly compressed plasma state and the kinetics of the dissociation, ionization, and nuclear D/D fusion reactions, which may take place near the center of the bubble. The numerical method used in our HYDRO code is summarized in Sec. VIII. In Sec. IX the hydrodynamic equations for a bubble cluster are given and a numerical simulation is presented. In Sec. X estimations for coalescence are given. Finally, in Sec. XI the salient results of the numerical simulations are presented and discussed.

II. EXPERIMENTAL STUDY OF BUBBLE FUSION

In cavitation experiments using chilled, deuterated acetone (Taleyarkhan *et al.*[1,2]), statistically significant tritium production along with 2.45 MeV neutron emissions indicated that D/D fusion had occurred. In the present section a brief description of the ORNL experiments and key results are presented.

Well-degassed deuterated (C_3D_6O) or natural (C_3H_6O) acetone liquid was placed in a cylindrical glass flask [i.e., the acoustic chamber (AC) of internal radius $R_{\mathrm{AC}}=32.5$ mm] and driven acoustically with an externally mounted piezoelectric transducer ring at a frequency be about $f_{\mathrm{AC}}=19.3$ kHz (i.e., the period of the acoustic oscillation was $t_{\mathrm{AC}}=51.8$ μs). The acoustic pressure amplitude in the central

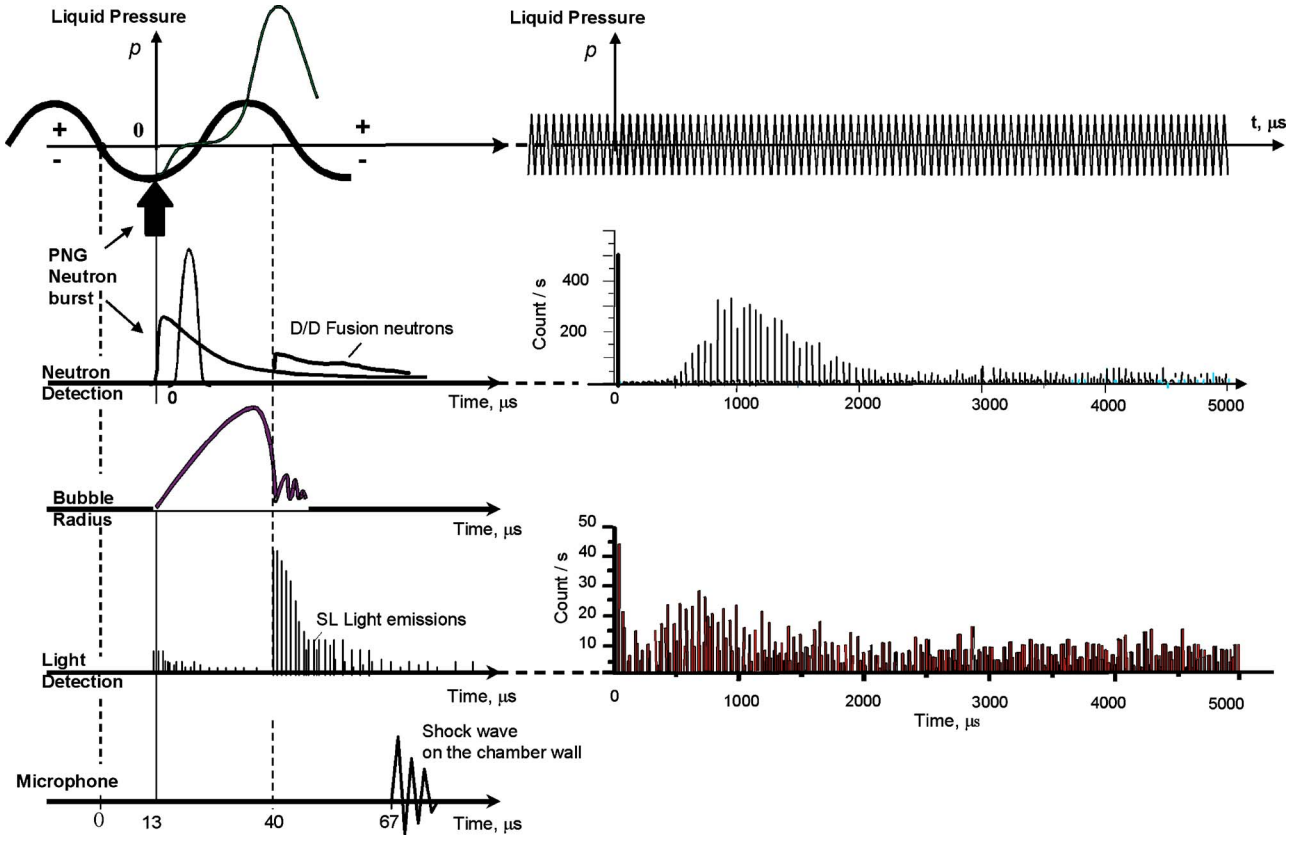

FIG. 1. (Color online). Schematic sequence of events during the ORNL bubble fusion experiments [Taleyarkhan *et al.* (Refs. 1 and 2)].

region of the chamber, where focusing of the acoustic waves took place, was typically $\Delta p \approx 15$ bars. After about 100 acoustic cycles (i.e., every 5000 μs), with a frequency of about $f_{\mathrm{PNG}}=200$ Hz, a pulsed neutron generator (PNG) emitted a burst of 14.1 MeV neutrons. This neutron pulse was short ($\Delta t \approx 10$ μs) and was coordinated with the acoustic wave generator so that it was emitted at the moment $\left(t \approx 12\ \mu\mathrm{s} \approx \frac{1}{4} t_{\mathrm{AC}}\right)$ of minimum liquid pressure (i.e., $p \approx -15$ bars) in the acoustic antinode. The neutrons interacting with the highly tensioned liquid nucleated a cluster of microvapor bubbles. However, since the PNG neutrons did not always interact with the liquid in the antinode, not every neutron pulse from the PNG produced a cluster. In fact, the frequency of the bubble clusters initiations were less than f_{PNG} and equaled $f_{\mathrm{CL}} \approx 50\ \mathrm{s}^{-1}$. The maximum radius of the bubble cluster was about $R \approx 4$ mm. To achieve this radius, the vapor bubbles in the cluster grew until the acoustic pressure in the liquid became positive $\left(t \approx \frac{1}{2} t_{\mathrm{AC}} \approx 26\ \mu\mathrm{s}\right)$. After that, during the compression period of the acoustic cycle, the bubbles began to collapse. This collapse was complete at $t \approx 40$ μs. If the implosion was robust enough, a SL light pulse was detected by a photomultiplier tube (PMT). If the vapor was composed of deuterium (D) atoms (i.e., D-acetone vapor), and the conditions were appropriate, 2.45 MeV D/D neutron production was also measured by a liquid scintillator.

As seen in Fig. 1, the neutrons are produced by cavitation not only after the first collapse ($t \approx 40$ μs), but after a dead-time interval of about ten acoustic periods (500 μs), the production of the neutrons resumed and became quasiperiodic during about $n' \approx 40-50$ bubble cluster bounces (see Fig. 1), which were coordinated with the acoustic forcing frequency and SL light emissions. It is interesting to note in Fig. 1 that the intensity of neutron emissions after $n' \approx 40-50$ bounces finally diminishes. This is presumably due to the fact that the Bjerknes force[20] expels the bubble cluster from the acoustic antinode, and condensation of the vapor bubble also occurs in the chilled liquid pool.

The number of energetic bubble cluster collapses and subsequent bounces per second, f, and the intensity of 2.45 MeV D/D neutron production, P, were[1,2]

$$f = n' f_{\mathrm{CL}} \approx (2.3 \pm 0.2) \times 10^3\ \mathrm{s}^{-1}, \quad P \approx (4 \pm 1) \times 10^5\ \mathrm{s}^{-1}. \tag{1}$$

It should be stressed that all of the D/D neutron pulses were emitted during a time interval in which the PNG was not operating. Indeed most of the D/D neutrons were emitted after a relatively long time interval, ~10 acoustic cycles (i.e., 500 μs), after the cluster was initiated by the PNG pulse ($\Delta t \approx 10$ μs). These neutrons were emitted during $n' \approx 40-50$ acoustically driven quasiperiodical bounces (i.e., a period of $t_{\mathrm{AC}}=51.8$ μs).

Moreover, when a bubble implodes with SL and neutron emissions, a pressure wave in the liquid is also generated, and these waves were detected[1,2] one acoustic transport delay (R_{AC}/C_L) after the neutron and SL light emissions. The detection of the waves was made at the chamber walls using

small pill microphones.[1,2] Also it was found that, together with the 2.45 MeV D/D neutron production, tritium (T) production took place as expected for D/D fusion. The measured[1,2] production of tritium nuclei (T) was at the same rate as for the 2.45 MeV neutron production, P.

Experiments were conducted at liquid pool temperatures of $T_0 \approx 273$ K and $T_0 \approx 293$ K, with and without acoustic forcing and irradiation with 14.1 MeV neutrons, with normal acetone, C_3H_6O, as the control fluid, and with deuterated acetone, C_3D_6O, as the test fluid. The products of D/D nuclear fusion (2.45 MeV neutrons and tritium, T) were detected only for the lowest pool temperatures (273 K), with acoustic forcing, in PNG-irradiated deuterated acetone.

In 1990 Lipson *et al.*[32] claimed a neutron production of low intensity, $P \sim 2$ n/s (compare with $P \approx 4 \times 10^5$ n/s in the experiments of Taleyarkhan *et al.*[1,2]) in MBSL experiments using a titanium vibrator in D_2O. This paper was not widely cited because of the low intensity of the neutron production (at the level of the background) and the absence of information on the measurement system used for the detection of neutrons and their energy.

III. THEORETICAL MODEL OVERVIEW

We omit from this paper the details concerning how the neutrons emitted by the PNG nucleate vapor bubbles in the tensioned liquid during the expansion phase of the acoustic wave, since this has been discussed elsewhere (Lahey *et al.*[5]). Thus, we start the simulations from the instant when a microbubble cluster has been created. A spherically symmetric approximation of the bubbles was used. In this approximation independent variables are the Eulerian radial coordinate, r, and time, t.

Since they are exposed to a negative ambient pressure (i.e., -15 bars) the cavitation bubbles rapidly grow. The bubbles are filled with vapor whose mass changes with time due to evaporation/condensation kinetics (see Sec. V). Bubble growth is slow relative to the speed of sound in the vapor. This is why a generalized low Mach number model of Rayleigh-Plesset (Sec. V) can be used to describe the liquid and vapor motion during bubble growth (Nigmatulin;[33] Nigmatulin and Khabeev,[34] Nigmatulin *et al.*,[35] Prosperetti, Crum, and Commander[36]). This stage takes almost all the time of the total process. During the low Mach number stage of bubble growth the pressure inside the bubble is essentially uniform, although the temperature is not, and an incompressible model for the surrounding liquid may be used. The bubbles grow until the increasing acoustic pressure in the liquid during the compression period of the acoustic cycle arrests bubble growth and causes them to contract. At the beginning of bubble collapse the velocity of vapor/liquid interface is still small relative to the vapor speed of sound, and the use of the low Mach number model remains appropriate.

To model the latter stages of the bubble implosion (and rebound), a high Mach number model (Sec. VII) based on a full set of fluid dynamics conservation equations, with interacting shock waves inside and outside of the bubble, molecular and ionic thermal conductivity, evaporation and condensation, and dissociation and ionization, was employed.

During the expansion period of the bubble, evaporation takes place keeping the vapor in the bubble near its saturation state. This leads to a nearly constant vapor pressure. During the implosion stage, the vapor starts to condense. It is important to note that during bubble collapse nonequilibrium condensation takes place. The faster the bubble implosion is, the farther the vapor is from thermodynamic equilibrium with the liquid, and thus the higher the pressure and temperature of the vapor. When the vapor pressure reaches the thermodynamic critical point, condensation stops. From this moment on the bubble contracts as if it were filled with a noncondensable high-density fluid. Hence, careful modeling of the evaporation/condensation process is important because it determines the amount of vapor in a collapsing bubble that will be further involved in the implosion process. During the high Mach number stage (this stage is very short ~ 0.5 μs, but needs the most effort for calculation) of bubble implosion, along with an almost adiabatic compression in the bubble's interior, compression shock waves are generated at the interface [i.e., at $r=a(t)$]. These shock waves converge and focus toward the center of the bubble. Due to this focusing the shock can compress and heat a very small central part of the bubble to extremely high values. Vapor molecules in this region will dissociate and ionize, creating a two-component, two-temperature plasma of ions and electrons giving rise to the plasma interactions that are discussed in Sec. VII and in Appendices E–G.

The compression rate of the plasma is very high and the ion temperature grows very fast. In contrast, the electrons do not have enough time to absorb much energy from the ions, and therefore they stay relatively cold and have negligible impact on the energy and momentum of the plasma due to a low absorption of energy from the ions and emission of light and thermal radiation. In particular, the energy losses associated with the electrons are relatively low. The ion temperature and density approach the conditions that are appropriate for a D/D reaction in a very small region during a very short time ($\sim 10^{-13}$ s) interval. The neutron yield due to thermonuclear fusion reactions is calculated using a neutron kinetics model presented in Sec. VII.

It should be noted that our model assumes the validity of an extended "hot-spot" model, where converging shock and compression waves create thermonuclear conditions near the center of the imploding bubbles. There are a number of other theories for sonoluminescence[20] and sonofusion. For example, Lipson, Kuznetsov, and Miley,[37] using the theory of Margulis[38] and Margulis and Margulis,[39] proposed that the light pulses and D/D fusion were associated with high-energy electrical sparks within the cavitation bubbles. This work is discussed and compared with the ORNL data in Ref. 40.

It should also be noted here that a realistic equations of state for the fluid (liquid, vapor, plasma), which accounts for the impact of liquid dissociation on its physical and thermodynamic properties, is crucial in the theoretical predictions of the experimentally observed bubble fusion. This is why we start the discussion of our theoretical results with a detailed description of the equations of state.

IV. EQUATIONS OF STATE

The key to achieving good predictions is the equations of state, which are valid during low and high compressions.

To distinguish the parameters of the different phases and components, subscript k will be used, where $k=L$ denotes the liquid, $k=G$ denotes gas/vapor, $k=m$ denotes molecular or nondissociated gas/vapor, $k=d$ denotes atomic dissociated gas (both nonionized and ionized), $k=d0$ denotes the dissociated but not ionized gas, and $k=1, 2, \ldots, z$ denotes dissociated and ionized gas with different levels of ionization.

The total number of electrons per molecule is Z_e. For acetone (C_3D_6O or C_3H_6O)

$$Z_e = 3 \times 6 + 6 \times 1 + 1 \times 8 = 32. \tag{2}$$

The number of binding energies of these Z_e electrons is Z. For acetone,

$$Z = 6 + 1 + 8 = 15. \tag{3}$$

The subscript S will be used to denote the saturation (vapor/liquid) state (e.g., $p_S, \rho_{LS}, \rho_{GS}$), and the subscript 0 will be used for the initial ($t=0$) state at rest (e.g., $a_0, p_0, T_0, \rho_{L0}, \rho_{G0}$.

A. Low pressure

During the stage of the bubble dynamics when the vapor density ρ and pressure p are not very high (i.e., $p<10$ bars), the gas/vapor parameters (density, ρ, pressure, p, temperature, T, and internal energy, ε) satisfy the perfect gas equation of state characterized by a heat capacity at constant volume, $c_G=c_m$ and adiabatic exponent, $\gamma_G=\gamma_m$ (where the subscript $m$denotes a molecular, nondissociated quantity):

$$\varepsilon = c_G T, \quad p = (\gamma_G - 1) c_G \rho T. \tag{4}$$

For D-acetone and H-acetone vapor (Vargaftik,[41] Beaton and Hewitt[42])

$$\begin{aligned} &\text{D-acetone:} \quad c_G = c_m = 1041 \text{ J/(kg K)}, \ \gamma_G = \gamma_m = 1.125, \\ &\text{H-acetone:} \quad c_G = c_m = 1148 \text{ J/(kg K)}, \ \gamma_G = \gamma_{mG} = 1.125. \end{aligned} \tag{5}$$

During this stage the liquid around the bubble may be treated as incompressible with constant density and constant heat capacity, c_L, thus,

$$\rho = \rho_{L0}, \quad \varepsilon = c_L T. \tag{6}$$

For liquid acetone (Vargaftik,[41] Beaton and Hewitt[42])

$$\text{D-acetone:} \quad \rho_{L0} = 858 \text{ kg/m}^3, \quad c_L = 1517 \text{ J/(kg K)}, \tag{7a}$$

$$\text{H-acetone:} \quad \rho_{L0} = 810 \text{ kg/m}^3, \quad c_L = 1517 \text{ J/(kg K)}. \tag{7b}$$

B. Saturation and thermodynamic critical state for vapor and liquid

For the higher pressures associated with the thermodynamic critical pressure, p_{cr}, when the temperature is comparable with the thermodynamic critical temperature, T_{cr}, it is necessary to take into account the influence of the temperature and pressure on the density of the liquid and that the vapor is not a perfect gas.

At the critical point (Vargaftik,[41] Beaton and Hewitt[42])

$$\begin{aligned} &\text{D-acetone:} \quad p_{cr} = 46.6 \text{ bars}, \quad T_{cr} = 508 \text{ K}, \\ &\qquad\qquad \rho_{cr} = 309 \text{ kg/m}^3, \\ &\text{H-acetone:} \quad p_{cr} = 46.6 \text{ bars}, \quad T_{cr} = 508 \text{ K}, \\ &\qquad\qquad \rho_{cr} = 280 \text{ kg/m}^3. \end{aligned} \tag{8}$$

The experimental fits for saturation temperature, $T_S(p)$, saturation pressure, $p_S(T)$, and the dependence of the latent heat on temperature, $h_{LG}(T)$, or equivalently on pressure, $h_{LG}(p)$, were used. The Clausius-Clapeyron equation was used to calculate the densities of liquid, $\rho_{LS}(p)$, and gas, $\rho_{GS}(p)$, on the saturation line (Nigmatulin[33]):

$$\frac{dT_S}{dp} = \frac{T_S(p)}{h_{LG}(p)} \left(\frac{1}{\rho_{GS}(p)} - \frac{1}{\rho_{LS}(p)} \right). \tag{9}$$

According to thermodynamic matching conditions for the internal energies of the vapor and liquid on the saturation line the following equation for vapor internal energy was used (Nigmatulin[33]):

$$\varepsilon_G(\rho_{VS}(T), T) = \varepsilon_L(\rho_{LS}(T), T) + h_{LG}(T) - p_S(T) \left(\frac{1}{\rho_{GS}(T)} - \frac{1}{\rho_{LS}(T)} \right), \tag{10}$$

where $\varepsilon_G(\rho_{GS}(T), T)$ and $\varepsilon_L[\rho_{LS}(T), T]$ are the values of internal energy of vapor and liquid on the saturation line, respectively.

The functions $p_S(T)$ and $h(T)$ were approximated according to experimental data (Vargaftik[41]) in the form

$$p_S(T) = p_* \exp\left(-\frac{T_*}{T} \right), \quad h_{LG}(T) = h_* \left(\frac{T_{cr}}{T} - 1 \right)^{0.37}, \tag{11}$$

$$T_* = 3700 \text{ K}, \quad p_* = 6.85 \times 10^9 \text{ Pa}, \quad h_* = 5.7 \times 10^5 \text{ J/kg}.$$

C. Equation of state for the high pressures and densities

To describe the thermodynamic properties of the liquid, vapor, and the condensed (i.e., supercritical) phases, the Mie-Gruneisen equation of state was used (Nigmatulin,[33] Altshuler,[43] Zeldovich and Raizer,[44] Walsh and Rice[45]). In this model the pressure, p, and the internal energy, ε, of a fluid were treated as the sum of potential ($p^{(p)}, \varepsilon^{(p)}$), thermal ($p^{(T)}, \varepsilon^{(T)}$), and latent chemical energy ($\varepsilon^{(ch)}$) components:

$$p = p^{(p)} + p^{(T)}, \quad \varepsilon = \varepsilon^{(p)} + \varepsilon^{(T)} + \varepsilon^{(ch)}. \tag{12}$$

It should be noted that the latent chemical energy may change due to phase transitions and chemical transformations.

The potential (or cold) components are responsible for the intermolecular, interatomic, or interion interactions in the fluid and are uniquely defined by the density of the fluid:

$$p^{(p)} = p^{(p)}(\rho) = \rho^2\left(\frac{\mathrm{d}\varepsilon^{(p)}}{\mathrm{d}\rho}\right), \quad \varepsilon^{(p)} = \varepsilon^{(p)}(\rho) = \int_{\rho^\circ}^{\rho} \frac{p^{(p)}(\rho)}{\rho^2}\mathrm{d}\rho. \tag{13}$$

Thermal components are responsible for the interactions because of the thermal motion of the molecules, atoms, ions, electrons, and photons. As is standard practice, the approximation of constant heat capacity and a Gruneisen coefficient Γ, which depends only on density, was used:

$$p^{(T)} = \rho\Gamma(\rho)\varepsilon^{(T)}, \quad \varepsilon^{(T)} = c\ T. \tag{14}$$

D. Dissociation and ionization of the gas/vapor phase

The dissociation and ionization process induces the following:

(1) Transformation of the structure of the substance and the intermolecular forces characterized by potential pressure $p^{(p)}(\rho)$ and the Gruneisen coefficient, $\Gamma(\rho)$.
(2) Transformation of the thermal motion of the ions and electrons making their motion independent. This increases the effective heat capacity of the substance, c.
(3) Absorption of energy due to the latent chemical energy component of internal energy, $\varepsilon^{(\mathrm{ch})}$.

To take these points into account, the substance was considered to be a mixture of two components—molecular (i.e., nondissociated, $k=m$) and atomic (dissociated, $k=d$) with different equations of states (12)–(14) and additive or equal pressures for components m and d:

$$\begin{aligned}
&\rho = \varphi_m\rho_m + \varphi_d\rho_d, \quad \varphi_m + \varphi_d = 1,\\
&p = \varphi_m p_m(\rho_m, T) + \varphi_d p_d(\rho_d, T) \quad \text{or}\\
&p = p_m(\rho_m, T) = p_d(\rho_d, T),\\
&\varepsilon = \chi_m\varepsilon_m(\rho_m, T) + \chi_d\varepsilon_d(\rho_d, T),\\
&\chi_m = \varphi_m\rho_m/\rho, \quad \chi_d = \varphi_d\rho_d/\rho,\\
&\varepsilon_k = \varepsilon_k^{(p)}(\rho_k) + c_k T + \varepsilon_k^{(\mathrm{ch})},\\
&p_k = p_k^{(p)}(\rho_k) + \rho_k\Gamma_k(\rho_k)c_k T \quad (k = m, d),
\end{aligned} \tag{15}$$

where subscript $k=m$ and d correspond to the nondissociated (molecular) or dissociated (atomic) components; φ_d and χ_d are the volume and mass fractions of dissociated gas ($\varphi_m = 1-\varphi_d, \chi_m = 1-\chi_d$). For our conditions both equations for the pressure, additive (with concentrations) partial pressures (i.e., $p=\varphi_m p_m + \varphi_d p_d$), that is appropriate for a homogeneous mixture of two rarefied gases, and the equality of partial pressures ($p=p_m=p_d$), that is appropriate for a heterogeneous (two-phase) mixture, gave practically the same results. However, sometimes the second model was more convenient for numerical evaluations.

For all gas/vapor states an approximation of constant Gruneisen coefficient was used. For the nondissociated ($k=m$) gas (vapor) state (see Fig. 4 later in this article), taking into account that the Gruneisen coefficient Γ corresponds to $\gamma-1$ [i.e., compare (4) and (14)], the heat capacity, c_G, and Gruneisen coefficient was the same as for the rarefied state in (5).

All other gas states (dissociated and ionized, $k=d, d0, 1, \ldots, Z$) correspond to a mixture of "monoatomic" gases. This mixture consists of atoms or ions of carbon C, deuterium D or hydrogen H, oxygen O and electrons. Because of the monoatomic structure the adiabatic exponent is $\gamma=\Gamma+1=1.667$. The heat capacity of the fully dissociated vapor was calculated as

$$C_d = 3/2nk^{(B)}, \quad \Gamma_d = 0.6667, \tag{16}$$

where $k^{(B)}=1.38\times10^{-23}$ J/K is the Boltzmann constant, and n is a number of atoms and ions per unit mass of the vapor. The number n is calculated by

$$n = \frac{\mathsf{N}^{(A)}}{M}Z_i, \tag{17}$$

where $\mathsf{N}^{(A)}=6.02\times10^{26}$ kmol^{-1} is the Avogadro number, M is the molecular weight of the gas, and Z_i is a number of ions or atoms per molecule. For acetone

$$\begin{aligned}
&\text{D-acetone}(C_3D_6O): \quad M = 64 \text{ kg/kmol}, \ Z_i = 10;\\
&\text{H-acetone}: \quad M = 58 \text{ kg/kmol}, \ Z_i = 10.
\end{aligned} \tag{18}$$

Thus,

$$\begin{aligned}
&\text{D-acetone}: \quad \Gamma_d = 0.667, \ c_d = 1947 \text{ J/(kg K)},\\
&\text{H-acetone}: \quad \Gamma_d = 0.667, \ c_d = 2148 \text{ J/(kg K)}.
\end{aligned} \tag{19}$$

The contribution of the electrons to the heat capacity of all ionized states is considered negligible because of the very short time of the fully ionized state ($10^{-13}-10^{-11}$ s) induced by a shock compression in the central zone of the microbubbles. During this short time interval the electrons do not have time to absorb much energy from the "hot" ions and the electron temperatures, T_e, are much less than the ion temperatures, T_i [i.e., $T_e \ll T_i$, see the discussion on (58)]. Such a nonequilibrium two-temperature plasma is conventionally called a "cold electron" plasma. It should be noted that the equilibrium heat capacity of a fully ionized plasma would be determined not by $Z_i=10$ but by $Z_i+Z_e=42$. Then the heat capacity would be 4.2 times larger [7983 J/(kg K)], and that would decrease the temperature of the fully ionized plasma by four times.

The so-called chemical part of the internal energy for the gas/vapor phase in the bubble was calculated taking into account the latent (evaporation/condensation) heat determining $\varepsilon_m^{(\mathrm{ch})}$, the energy of dissociation $\varepsilon_d^{(\mathrm{ch})}$ of the molecule, and the energy of ionization $\varepsilon_i^{(\mathrm{ch})}$, depending on the levels, χ_k, of all types of electron excitation states ($k=d0,1,2,\ldots,Z$) and the corresponding chemical energies (potential for ionization) $\varepsilon_k^{(\mathrm{ch})}$ for all atoms in the molecule (see Babichev, Babushkina, and Bratkovsky[46]):

$$\varepsilon_G^{(\mathrm{ch})} = \varepsilon_m^{(\mathrm{ch})} + \chi_d(\varepsilon_d^{(\mathrm{ch})} + \varepsilon_i^{(\mathrm{ch})}), \quad \varepsilon_i^{(\mathrm{ch})} = \sum_{k=1}^{Z} \chi_k \varepsilon_k^{(\mathrm{ch})},$$
$$\chi_{d0} + \sum_{k=1}^{Z} \chi_k = \chi_d. \tag{20}$$

The constant chemical constituent of the internal energy for a nondissociated molecular gas/vapor $(k=m)\varepsilon_m^{(\mathrm{ch})}$ was chosen to make the internal energies of the liquid $(k=L)$ and vapor $(k=m)$ equal at the critical point. For lower temperatures and pressures it was in good agreement with the latent heat, $h_{\mathrm{LG}}(T)$.

For D-acetone the energy required for dissociation is shown in Appendix A to be

$$\varepsilon_d^{(\mathrm{ch})} = 28.2 \times 10^6 \text{ J/kg}. \tag{21}$$

The latent energy of ionization, $\varepsilon_i^{(\mathrm{ch})}$, was calculated taking into account the binding energies of all $Z=15$ types of electrons in the D-acetone molecule. This molecule has one electron in each of six deuterium atoms $(k=\mathrm{D1})$, six electrons in each of three carbon atoms $(k=\mathrm{C1, C2, C3, C4, C5, C6})$, and eight electrons in one oxygen atom (O1, O2, O3, O4, O5, O6, O7, O8). Each of these $Z=15$ types of $Z_e=32$ electrons in one acetone molecule has its own binding energy $\varphi_k \equiv \mathsf{k}^{(\mathsf{B})} T_k (k=1,2,\ldots,Z=14)$ that is determined by the ionization temperature, T_k and the Boltzmann constant $\mathsf{k}^{(\mathsf{B})}$.

The level of ionization, χ_k, is the ionization fraction of kth-type electrons, ν_k is number of the corresponding atoms in the molecule C_3D_6O $(\nu_{\mathrm{D}}=\nu_{\mathrm{D1}}=6, \nu_{\mathrm{C}}=\nu_{\mathrm{C1}}=\nu_{\mathrm{C2}}=\ldots=\nu_{\mathrm{C6}}=3, \nu_{\mathrm{O}}=\nu_{\mathrm{O1}}=\nu_{\mathrm{O2}}=\ldots=\nu_{\mathrm{O8}}=1)$. Then the chemical component of internal energy due to ionization is

$$\varepsilon_i^{(\mathrm{ch})} = \sum_{k=1}^{Z} \frac{\mathsf{N}_A \nu_k}{M} \chi_k \varphi_k = \frac{\mathsf{R}}{M} \left\{ 6T_{\mathrm{D1}}\chi_{\mathrm{D1}} + 3\sum_{k=\mathrm{C1}}^{\mathrm{C6}} T_k \chi_k + \sum_{k=\mathrm{O1}}^{\mathrm{O8}} T_k \chi_k \right\}, \tag{22}$$

where M is the molecular weight $(M=64 \text{ kg/kmol})$ and $\mathsf{R}=8314 \text{ J/(kmol K)}$ is the universal gas constant. All values of T_k for acetone are given in Appendix A. The full energy of ionization (i.e., all $\chi_k=1$ for $k=1,2,\ldots,15$) of D-acetone is

$$\varepsilon_i^{(\mathrm{ch})} = 7.663 \times 10^9 \text{ J/kg}. \tag{23}$$

Keeping in mind that the value of heat capacity for the D-acetone plasma [see (19)] is $c=1947[\mathrm{J/(kg \times K)}]$, the energy of full ionization corresponds to $\varepsilon_i^{(\mathrm{ch})}/c \approx 3.9 \times 10^6$ K. This means that dissociation and ionization dynamics is crucial when the temperature is less than 10^7 K (e.g., for MBSL and SBSL) but it is not essential when $T \geqslant 10^8$ K (recall the discussion on Didenko's and Suslik's[31] criticism of the experiments of Taleyarkhan *et al.*[1] in Sec. I). Nevertheless, the dissociation and ionization process during other lower temperature processes (e.g., heat transfer, evaporation, condensation) plays a role in the gas dynamics before the fusion core formation, and thus they must be carefully evaluated.

The model given by Eqs. (15)–(23) provides for a continuous transition from the nondissociated and nonionized molecular state to the dissociated and then ionized state by transition of the equations of states for a molecular gas/vapor $(k=m)$ to the equations of state for a dissociated and ionized vapor. There will be various levels of dissociation and ionization (x_k) because of increasing temperature T due to a compression wave, or decreasing temperature T and levels of dissociation and ionization (x_k) due to a rarefaction wave. At the same time this model allows for the absorption of energy due to increasing the latent chemical energy, $\varepsilon_G^{(\mathrm{ch})}$, when the temperature and levels of dissociation and ionizations (x_k) increase, and a release of the latent chemical energy, $\varepsilon_G^{(\mathrm{ch})}$, when temperature and levels of dissociation and ionizations (x_k) decrease.

E. Approximation for the potential pressure and potential internal energy

To model the elastic (i.e., cold) potentials $p^{(p)}(\rho)$, $\varepsilon^{(p)}(\rho)$, which describe the elastic interactions between the atoms at zero temperature $(T=0 \text{ K})$, we have used a generalized Born-Mayer potential, which accounts for the intermolecular attraction-repulsion forces in condensed matter (Nigmatulin,[33] Born and Mayer,[47] Zharkov and Kalinin,[48] Jacobs,[49] Cowperthwaite and Zwisler,[50]):

$$p^{(p)}(\rho) = A\tilde{\rho}^{-\beta+1} \exp[b(1-\tilde{\rho}^{-\beta})] + E\tilde{\rho}^{\alpha+1} - K\tilde{\rho}^{\xi+1} + \Delta p^{(p)}, \tag{24}$$

$$\varepsilon^{(p)}(\rho) = \frac{A}{\beta\rho_0 b}\exp[b(1-\tilde{\rho}^{-\beta})] + \frac{E}{\alpha\rho_0}\tilde{\rho}^{\alpha} - \frac{K}{\xi\rho_0}\tilde{\rho}^{\xi} + \Delta\varepsilon^{(p)} + \varepsilon^{\circ} \quad \left(\tilde{\rho} \equiv \frac{\rho}{\rho_0}\right). \tag{25}$$

Here $A, K, E, b, \xi, \alpha, \beta$ are constants, $\Delta p^{(p)}(\rho)$ is a correction term used for very high fluid density (i.e., larger than $2.5\rho_{L0}$) or relatively low fluid density (i.e., smaller than $0.3\ \rho_{L0}$). The numerical values of these parameters are given in Appendix B.

In the two-phase region, ε° is an integration constant of potential energy, chosen to satisfy

$$\varepsilon^{(p)}(\rho^{\circ}) = 0, \tag{26}$$

ρ° is the fluid density when the elastic pressure is zero $[p^{(p)}(\rho^{\circ})=0]$, and a minimum value of the potential energy of the fluid is achieved.

Often the potential in (24) and (25) without an exponential term $(A=0)$ has been used and it is called the Lennard-Jones potential. However, for extremely high compression of solids and fluids the exponential term is important. Also the parameters E and α have been found to improve the agreement with the data for lower densities, $\rho < 0.3\rho_{L0}$.

The problem was to generalize the potentials in (24) and (25) in both the vapor and liquid phases and the two-phase (vapor/liquid) region.

In our analysis a simplified constant heat capacity approximation for liquid and for vapor was used. In this approximation there are two different heat capacities $c_G=c_m$ and c_L for the two molecular phases. We must use two different approximations for the elastic potentials in (24) and

(25) for the molecular substance (D-acetone). The first is for the molecular D-acetone liquid $(p_L^{(p)}, \varepsilon_L^{(p)})$ with coefficients $A_L, b_L, \beta_L, K_L, E_L, \alpha_L, \xi_L$, and with Gruneisen coefficient and heat capacity (Γ_L, c_L). The second is for the molecular D-acetone vapor $(p_m^{(p)}, \varepsilon_m^{(p)})$ with coefficients $A_m, b_m, \beta_m, K_m, E_m, \alpha_m, \xi_m$, and with Gruneisen coefficient and heat capacity (Γ_m, c_m). A third elastic potential is used for the dissociated D-acetone fluid $(p_d^{(p)}, \varepsilon_d^{(p)})$ with coefficients $A_d, b_d, \beta_d, K_d, E_d, \alpha_d, \xi_d$, and with Gruneisen coefficient and heat capacity (Γ_d, c_d) for all ionized states (see Appendix B for details).

F. Algorithm for the calculation of the constants for the potential pressure and Gruneisen coefficient

In order to adequately predict the behavior of a fluid under strong compression (liquid or vapor phases) as well as at large specific volumes (vapor phase), one must use appropriate experimental data to evaluate the parameters in (24) and (25).

These parameters were chosen to match the calculated and experimental data for acetone for shock-induced and isothermal compressibility, and for the saturation pressure, latent heat, and densities of the liquid and vapor phases at saturation.

Let us consider the shock (Hugoniot) adiabat, which can be derived from the mass, momentum, and energy conservation laws across the shock (jump) wave (Landau and Lifshitz,[51] Rakhmatulin,[52] Zeldovich and Raizer,[44] Walsh and Rice,[45] Duderstadt and Moses[53]):

$$\rho_{L0} D = \rho (D - U), \quad \rho_{L0} D U = p - p_0,$$
$$\rho_{L0} D\left(\varepsilon + \tfrac{1}{2} U^2 - \varepsilon_0\right) = pU. \tag{27}$$

Here $\rho_{L0}, p_0, \varepsilon_0$ and ρ, p, ε are the density, pressure, internal energy before (subscript 0) and after (no subscript) the shock wave, D and U are the shock wave velocity and velocity of the material (liquid) behind the shock wave, respectively. Both velocities D and U are taken relative to the liquid at rest in front of the shock wave (i.e., $U_0 = 0$).

In experiments with condensed substances (solids and liquids) the velocity of a shock wave, D, and the velocity of the material after the shock wave, U, were measured for different intensities of the shock in the different substances. As a result the kinematic shock adiabat, $D(U)$, for the substance may be obtained. Using the conservation equations (27), the kinematic shock adiabat for the substance is easily recalculated as an experimental shock adiabat $p(\rho)$ characterizing the shock-induced compressibility of the substance (Nigmatulin,[33] Altshuler,[43] Zeldovich and Raizer,[44] Walsh and Rice[45]).

For all condensed substances it has been found that the shock adiabat line, $D(U)$, is close to linear:

$$D = C_0 + k_0 U, \tag{28}$$

where the intercept, C_0, is the sound speed, and k_0 is the slope. For some substances a change in the slope, k_0, and transition to another linear function takes place. This is associated with a physical or chemical transformation (e.g., a phase transition due to changing of crystal structure, chemical reaction, dissociation of the molecules, etc.) induced by strong shock wave compression and heating.

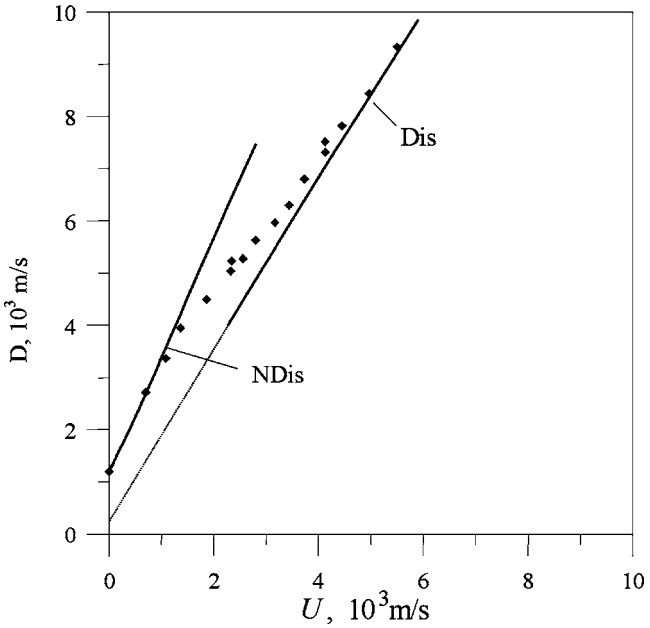

FIG. 2. The shock adiabat of liquid acetone in D, U coordinates; the dots correspond to experiments by Trunin *et al.* (Refs. 54 and 55), the labels NDis and Dis correspond to the nondissociated and dissociated states behind the shock wave, respectively.

For organic liquids, in particular, for acetone, the correlation $D(U)$ was measured by Trunin *et al.*[54,55] and is presented in Fig. 2. It is seen that there is a change of the slope when $U > 1.8$ km/s ($p > 61$ kbars). The corresponding chemical transformation is dissociation of the acetone mol-

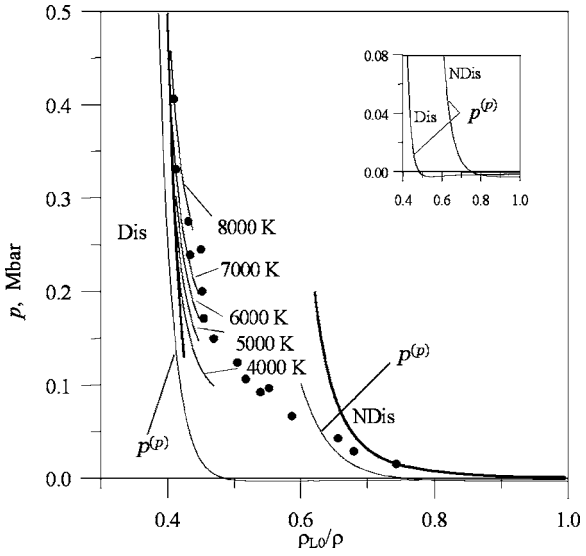

FIG. 3. The shock adiabats (solid lines) and calculated isotherms (thin lines) for liquid acetone in p, ρ coordinates. The solid lines labeled by NDis and Dis correspond to straight lines in Fig. 2; the dots correspond to the experimental data for the shock adiabat [Trunin *et al.* (Refs. 54 and 55)] in Fig. 2.

ecule. Significantly, shock-induced transformations in condensed substances requires a relaxation time (Zeldovich and Raizer,[44] Nigmatulin[33]) of

$$\tau_d > 10^{-7}\ \mathrm{s}. \tag{29}$$

In Fig. 2 the shock adiabat for lower intensity, $U < 1.8$ km/s ($p < 61$ kbars) is for nondissociated acetone and this straight line is marked by the label "NDis." The straight line for higher intensity ($U > 4.0$ km/s, $p > 200$ kbars), marked by the label "Dis," corresponds to full dissociation of the acetone molecule. Intermediate intensities ($1.8 < U < 4.0$ km/s, $61 < p < 200$ kbars) correspond to partial dissociation by the shock wave.

The correlation given in (28) for the two straight line parts of the shock adiabat, $D(U)$, for nondissociated and dissociated acetone are approximated by the following values of C_0 and k_0:

$$\text{Nondissociated (NDis):} \quad C_0 = C_{L0} = 1.189\ \mathrm{m/s}, \quad k_0 = k_{L0} = 2.25, \tag{30a}$$

$$\text{Dissociated (Dis):} \quad C_0 = C_{\mathrm{LD}} = 300\ \mathrm{m/s}, \quad k_0 = k_{\mathrm{LD}} = 1.62. \tag{30b}$$

The two experimental shock adiabat lines, $p_{\mathrm{sh}}(\rho)$, for acetone (initially at STP conditions: $p_0 = 1$ bars, $T_0 = 293$ K before the shock wave) without and with dissociation (after the shock wave) and labeled by "NDis" and "Dis," are shown by the dark solid lines in Fig. 3.

The theoretical shock adiabat, $p(\rho)$, may be derived from the shock wave's conservation equations (27) and equations of state (12)–(14). This reduces to (Zeldovich and Raizer,[44] Nigmatulin[33])

$$p_{\mathrm{sh}}(\rho) = \frac{\dfrac{2}{\Gamma(\rho)} p^{(p)}(\rho) + p_0\left(\dfrac{\rho}{\rho_{L0}} - 1\right) - 2\rho\left(\varepsilon^{(p)}(\rho) - \varepsilon^{(p)}(\rho_{L0}) - \varepsilon_{L0}^{(T)}\right)}{1 + \dfrac{2}{\Gamma(\rho)} - \dfrac{\rho}{\rho_{L0}}}. \tag{31}$$

For the liquid phase it is possible to use a simplified Born-Mayer potential corresponding to $E = 0, \xi = 1$.

The Gruneisen coefficient for the nondissociated liquid acetone ($k = L$) can be approximated by

$$\Gamma(\rho) = a^{(0)} + a^{(1)} \exp\left[-\left(\frac{\rho}{\rho^{(1)}}\right)^{8/5}\right] + a^{(2)} \exp\left[-\left(\frac{\rho}{\rho^{(2)}}\right)^{-9/4}\right], \tag{32}$$

where

$$a^{(0)}, a^{(1)}, a^{(2)}, \rho^{(1)}, \rho^{(2)} \tag{33}$$

are constant coefficients that should be determined with

$$A, K, E, b, \xi, \alpha, \beta \tag{34}$$

in the formulas for $p^{(p)}(\rho), \varepsilon^{(p)}(\rho)$. All 12 of these constant coefficients were calculated to minimize the mean square deviation of pressure $p_{\mathrm{sh}}(\rho)$, given by (31), from the experimental shock adiabat, $p_{\mathrm{sh}}(\rho)$, following from $D(U)$ (in particular at the initial state) and the calculated density of the liquid on the saturation curve, $\rho_{\mathrm{LS}}(T)$ (in particular at the critical point) from the experimental data. Doing so it is useful to note that at the STP state ($T = T_0 = 293$ K, $p = p_0 = 10^5$ Pa, $\rho = \rho_{L0}$) Eqs. (14), (24), and (25) for pressure lead to

$$A - K + \rho_{L0}\Gamma(\rho_{L0}) c_L T_0 = p_0. \tag{35}$$

Using the experimental value for the speed of sound in liquid under STP conditions, one can find one more equation involving the parameters $A, K, b, \Gamma(\rho_{L0})$ and $\Gamma'(\rho_{L0})$, which is determined by the equation for the adiabatic speed of sound (Nigmatulin[33]) at the initial (STP) conditions. The speed of sound squared is given by the derivative $(\mathrm{d}p_{\mathrm{sh}}/\mathrm{d}\rho)$ along the shock adiabat (31) for the initial (STP) state, yielding

$$C_{L0}^2 = \frac{A}{3\rho_{L0}}(b-4) - c_{L0}T_0(\Gamma_0^2 + \Gamma_0'\rho_{L0} - \Gamma_0) + \frac{2p_0}{\rho_{L0}},$$

$$\left(\Gamma_0 = \Gamma(\rho_{L0}), \quad \Gamma_0' \equiv \Gamma'(\rho_{L0}) \equiv \left.\frac{\mathrm{d}\Gamma}{\mathrm{d}\rho}\right|_{\rho=\rho_{L0}}\right). \tag{36}$$

For the liquid D-acetone: $\rho_{L0} = 858\ \mathrm{kg/m^3}$ [see (7)], $C_{L0} = 1.189$ m/s [see (30a)].

Finally, one needs to use three conditions at the critical point (8):

$$p_{\mathrm{cr}} = p(\rho_{\mathrm{cr}}, T_{\mathrm{cr}}), \quad \left(\frac{\partial p}{\partial \rho}\right)_T = 0, \quad \left(\frac{\partial^2 p}{\partial \rho^2}\right)_T = 0. \tag{37}$$

Thus, in the most general case the approximation problem is reduced to varying seven independent coefficients among 12 coefficients (33) and (34) to obtain a correlation of the experimental shock adiabat shown in Fig. 3, with the theoretical shock adiabat, (31), and to get a correlation of the experimental saturation density $\rho_{\mathrm{LS}}(p)$ with the theoretical $\rho_{\mathrm{LS}}(p) = \rho_L[p, T_S(p)]$.

An analogous procedure was used for the gas/vapor molecular phase with saturation density $\rho_{\mathrm{GS}}(T)$ and critical

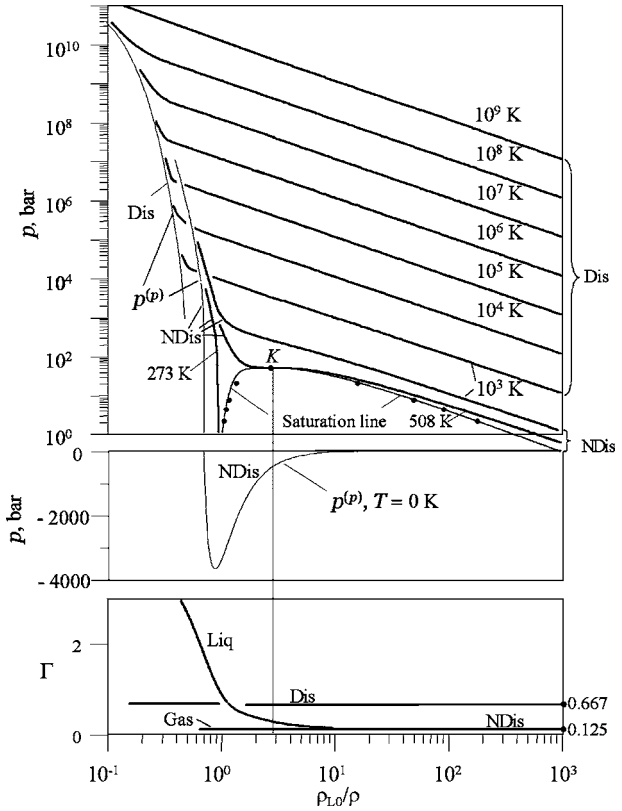

FIG. 4. A plot of the equation of state for D-acetone in logarithmic p,ρ coordinates at different temperatures. Isotherms $T=273$, 508, 10^3 K correspond to the molecular phase (NDis); the isotherms for $T\geqslant 1000$ K correspond to the dissociated phase (Dis). The dots are the experimental data for the liquid and vapor densities, $\rho_{LS}(p)$ and $\rho_{GS}(p)$, for saturation conditions, $T=T_S(p)$. The two zero isotherms ($T=0$ K) for nondissociated and dissociated acetone corresponding to the cold pressure, $p^{(p)}(\rho)$, and the saturation lines, $\rho_{LS}(p)$ and $\rho_{GS}(p)$, are shown, where K is the critical point. On the lower plots the negative part for the "cold" pressure $p^{(p)}(\rho)$ and Grüneisen coefficients, $\Gamma(\rho)$, for nondissociated liquid, and both dissociated and nondissociated vapor are shown.

point, keeping in mind that for high compression ($\rho/\rho_{L0}>2$) the elastic potentials for liquid and gaseous acetone should be asymptotically identical.

All details are given in Appendix B. In Fig. 4 the isotherms $p(\rho)$ are presented for nondissociated (Ndis) and dissociated (Dis) D-acetone for different temperatures, T, corresponding to our calculations. In particular, the isotherms for $T=0$ K are the potential (cold) pressures $p^{(p)}(\rho)$ for nondissociated and dissociated acetone.

V. LOW MACH NUMBER BUBBLE DYNAMICS

For the low Mach number stage when the radial velocity in the vapor, w, is much smaller than the speed of sound in the vapor, C_G, i.e., $\mathrm{M}\equiv|w|/C_G<\mathrm{M}_*$ ($\mathrm{M}_*\approx 0.05$–0.2), a homobaric (i.e., quasistatic approximation without inertial forces) approximation for the vapor inside the bubble and an incompressibility condition for the surrounding liquid may be used (see Appendix C). These assumptions and approximations have been verified using full HYDRO code simulations (see Sec. VII). Moreover, it has been shown numerically that the results are not sensitive to slight changes in the transition Mach number threshold, M_*, or equivalently, a transition interfacial acceleration.[56]

These two assumptions and approximations (homobaricity in gas and noncompressibility of the liquid for the low Mach noncollapsing stage, see Appendix C) were explicitly formulated and investigated previously by Nigmatulin[33] and by Nigmatulin and Khabeev[35] and by Lin, Storey, and Szeri.[56] As noted previously, these models have been verified using full HYDRO code simulations (see Sec. VII).

In a homobaric asymptotic model the gas/vapor pressure inside the bubble $[r<a(t)]$ is spatially uniform, but time dependent. The gas/vapor can be assumed to be a rarefied ($p^{(p)}\ll p^{(T)}$) perfect gas, (4), and the liquid can be assumed to be an incompressible fluid, (6). The density, ρ, temperature, T, and radial velocity, w, of the vapor are functions of time, t, and radial coordinate, r. A mathematical model describing the low Mach number period of bubble dynamics with thermal conductivity, nonuniform temperature, nonuniform vapor density, and phase transitions was proposed by Nigmatulin[33] and by Nigmatulin and Khabeev[34] and was successfully used for the analysis of SBSL by Nigmatulin *et al.*,[35] by Prosperetti, Crum, and Commander,[36] and by Lin, Storey, and Szeri:[56]

$r<a$:

$$\frac{\gamma_G p}{(\gamma_G-1)T}\left(\frac{\partial T}{\partial t}+w\frac{\partial T}{\partial r}\right)=\frac{1}{r^2}\frac{\partial}{\partial r}\left(\lambda_G r^2\frac{\partial T}{\partial r}\right)+\frac{\mathrm{d}p}{\mathrm{d}t}, \tag{38}$$

$$w=\frac{(\gamma_G-1)}{\gamma_G p}\lambda_G\frac{\partial T}{\partial r}-\frac{r}{3\gamma_G p}\frac{\mathrm{d}p}{\mathrm{d}t}. \tag{39}$$

Here λ_G is the temperature-dependent thermal conductivity coefficient of the gas/vapor phase.

In the region around the bubble the liquid can be treated as nearly incompressible because its density does not deviate significantly from its initial value. In this case the liquid velocity distribution in the so-called "liquid drop" region surrounding the bubble is taken as an exact solution of the liquid continuity equation for an incompressible liquid, and the momentum equation is reduced to the Bernoulli integral (Landau and Lifshitz,[51] Rakhmatulin,[52] Lamb,[57] Sedov,[58] Batchelor[59]). Then the equations for the distribution of radial velocity, w, pressure, p, and temperature, T, in the liquid ($r>a$) are

$$p(t,r)=p_{La}(t)-\rho_{L0}\left(a\frac{\mathrm{d}w_{La}}{\mathrm{d}t}+2\frac{\mathrm{d}a}{\mathrm{d}t}w_{La}-\frac{w_{La}^2}{2}\right)+\frac{\rho_{L0}}{r}\frac{\mathrm{d}}{\mathrm{d}t}(a^2w_{La})-\frac{\rho_{L0}a^4}{2r^4}{w_{La}}^2, \tag{40}$$

$$w_L=\frac{w_{La}a^2}{r^2}, \tag{41}$$

$$c_L\rho_{L0}\left(\frac{\partial T}{\partial t}+w\frac{\partial T}{\partial r}\right)=\frac{1}{r^2}\frac{\partial}{\partial r}\left(\lambda_L r^2\frac{\partial T}{\partial r}\right), \tag{42}$$

where p_{La} and w_{La} are pressure and radial velocity of the liquid at the interface $[r=a(t)]$, and λ_L is the temperature-

dependent thermal conductivity of the liquid.

Experimental data for the thermal conductivities for the gas ($k=G$) and liquid ($k=L$) acetone[41,42] were approximated by

$$\lambda_k = \lambda_k^\circ[1 + \Lambda_k^\circ((T/T^\circ)^\theta - 1)], \quad k = G,L$$

$$\lambda_G^\circ = 0.823 \times 10^{-2}\ \text{W/(m} \times \text{K)}, \quad T^\circ = 273\ \text{K},$$

$$\Lambda_G^\circ = 7.49, \quad \theta = 0.5, \tag{43}$$

$$\lambda_L^\circ = 0.169\ \text{W/(m} \times \text{K)}, \quad T^\circ = 273\ \text{K},$$

$$\Lambda_L^\circ = -0.609, \quad \theta = 1.0.$$

The instantaneous bubble radius, $a(t)$, is defined by a generalized Rayleigh-Plesset equation that takes into account acoustic radiation by the bubble due to liquid compressibility and the effect of mass transfer through the bubble's interface due to evaporation/condensation (Nigmatulin,[33] Nigmatulin *et al.*,[34,35,60] Prosperetti, Crum, and Commander[36]):

$$a\frac{\mathrm{d}w_{La}}{\mathrm{d}t} + \frac{3}{2}w_{La}^2 + 2\frac{w_{La}j}{\rho_{L0}} = \frac{p_{La} - p_I}{\rho_{L0}} + \frac{a}{\rho_{L0}C_{L0}}\frac{\mathrm{d}}{\mathrm{d}t}(p_{La} - p_I), \tag{44}$$

where $p_I(t)$ is the incident acoustic pressure from the far field.

The liquid and vapor velocities at the bubble's interface (w_{La} and w_{Ga}) and the radial velocity of the interface ($\dot{a} = \mathrm{d}a/\mathrm{d}t$) differ somewhat due to phase transition (evaporation/condensation). This fact is taken into account by the following mass jump conditions at the interface:

$$\dot{a} = w_{Ga} + \frac{j}{\rho_{Ga}} = w_{La} + \frac{j}{\rho_{La}}, \tag{45}$$

where j is evaporation flux, which is negative if condensation takes place, and ρ_{Ga} and ρ_{La} are densities of gas/vapor and liquid on the interface, respectively.

Similarly, using the momentum jump condition relates the vapor and liquid pressure at the interface,

$$p_{Ga} = p_{La} + \frac{2\sigma}{a} + \frac{4\mu_L w_{Ga}}{a}, \tag{46}$$

where σ is the surface tension, and μ_L is the dynamic viscosity of the liquid. These parameters were determined from available experimental data. In particular, for liquid acetone[41,42] we used the following approximation of the data:

$$\sigma = \sigma^\circ - \sigma' \ln(T/T^\circ), \quad \sigma^\circ = 0.028\ \text{N/m}, \quad \sigma' = 0.044\ \text{N/m}, \tag{47}$$

$$\mu_L = \mu^\circ \exp(-\chi T/T^\circ), \quad \mu^\circ = 0.54 \times 10^{-2}\ \text{Pa s}, \quad \chi = 2.56.$$

VI. EVAPORATION AND CONDENSATION KINETICS

To describe the evaporation/condensation processes at the interface [i.e., at $r=a(t)$] for both the low and high Mach stages, the energy jump condition was used:

$$\lambda_L \left.\frac{\partial T}{\partial r}\right|_{r=a+0} - \lambda_G \left.\frac{\partial T}{\partial r}\right|_{r=a-0} = j h_{\mathrm{LG}}(p_G a), \tag{48}$$

where j is the mass flux due to phase change [see (45)].

Analysis of the transport process of the vapor molecules at a liquid/vapor interface was based on the Hertz-Knudsen-Langmuir formula (Nigmatulin,[33] Volmer,[61] Schrage,[62] Kucherov and Rikenglaz[63]) which, after some simplifications, is given by (see Appendix D)

$$j = f\frac{p_S(T_a) - p_{Ga}}{\sqrt{2\pi(\mathsf{R}/M)T_a}}, \quad f = \frac{2\alpha}{(2-\alpha)}, \tag{49}$$

where α is the accommodation coefficient (e.g., the condensation/evaporation coefficient) that defines that portion of the vapor molecules hitting the liquid/vapor interface that are absorbed, the remaining portion, $(1-\alpha)$, being reflected. This equation represents an explicit formula for the evaporation ($j>0$) and condensation ($j<0$) rate, where f is an effective accommodation coefficient. It is easy to see that for very small α there is no difference between α and f, but if $\alpha=1$ (which corresponds to a maximum value for the accommodation coefficient), $f=2$.

There is a very small amount of data for α. However, for water, $\alpha \approx 0.04$, and it is known that for large and complicated molecules α is much larger (Volmer,[61] Schrage,[62] Paul[64]). In particular, for large organic molecules the accommodation coefficient is much larger than for water (i.e., $\alpha > 0.1$). This is one of the reasons why organic liquids are better than water for the supercompression of the bubbles (i.e., they have higher condensation rates and thus less vapor cushioning during implosions). For acetone we used $\alpha = 0.2-1.0$ (Paul[64]), and to investigate the influence also we made the calculations for other lower α.

VII. THE HIGH MACH NUMBER AND THE PLASMA STAGE

Let us now consider the equations of motion that comprise the HYDRO code. In the absence of significant viscous and diffusion processes, but taking into account thermal conductivity, the one-dimensional conservation equations for the conservation of mass, momentum, and energy in spherical coordinates are (Landau and Lifshitz,[51] Rakhmatulin,[52] Sedov[58])

$$\frac{\partial \rho}{\partial t} + \frac{1}{r^2}\frac{\partial}{\partial r}\left(r^2 \rho w\right) = 0, \tag{50}$$

$$\frac{\partial \rho w}{\partial t} + \frac{1}{r^2}\frac{\partial}{\partial r}\left(r^2 \rho w^2\right) + \frac{\partial p}{\partial r} = 0, \tag{51}$$

$$\frac{\partial}{\partial t}\left[\rho\left(\varepsilon + \frac{w^2}{2}\right)\right] + \frac{1}{r^2}\frac{\partial}{\partial r}\left\{r^2 w\left[\rho\left(\varepsilon + \frac{w^2}{2}\right) + p\right]\right\} = \frac{1}{r^2}\frac{\partial}{\partial r}\left(\lambda r^2 \frac{\partial T}{\partial r}\right). \tag{52}$$

A. Conservation equations for the plasma state

A more general one-dimensional equation for momentum conservation for a plasma is, in spherical coordinates,

$$\frac{\partial \rho w}{\partial t} + \frac{1}{r^2}\frac{\partial}{\partial r}(r^2 \rho w) + \frac{\partial}{\partial r}(p_i + p_e + p_r) = 0, \tag{53}$$

where p_i, p_e, p_r are the pressures of the ions, electrons and radiation (i.e., photons), respectively.

The corresponding energy conservation equation is

$$\frac{\partial}{\partial t}\left[\rho(\varepsilon_i + \varepsilon_e) + e_r + \frac{\rho w^2}{2}\right] + \frac{1}{r^2}\frac{\partial}{\partial r}\left\{r^2 w\left[\rho\left(\varepsilon_i + \varepsilon_e + \frac{w^2}{2}\right) + e_r + p_i + p_e + p_r\right]\right\} = \frac{1}{r^2}\frac{\partial}{\partial r}\left[r^2(q_i + q_e + S_r)\right], \tag{54}$$

where $\varepsilon_i, \varepsilon_e, e_r$ are the specific internal energies of the ions and electrons, and the radiation (i.e., photon) energy, respectively; q_i, q_e, S_r are the ion and electron heat fluxes and the flux of radiation energy, respectively.

Since $T_i \neq T_e$, it is normally necessary to derive separate conservation equations for the electrons. That is, we can formulate the mass, momentum, and energy conservation laws for the electron gas coupled with the associated radiation terms:

$$\frac{\partial \rho_e}{\partial t} + \frac{1}{r^2}\frac{\partial}{\partial r}\left(r^2 \rho_e w_e\right) = \Psi_{ie} m_e \quad (\rho_e = n_e m_e), \tag{55}$$

$$\rho_e \frac{\mathrm{d}_e w_e}{\mathrm{d}t} = -\frac{\partial}{\partial r}(p_e + p_r) + f_{ie} \quad \left(\frac{\mathrm{d}_e}{\mathrm{d}t} = \frac{\partial}{\partial t} + w_e \frac{\partial}{\partial r}\right), \tag{56}$$

$$\frac{\partial}{\partial t}\left[\rho_e\left(\varepsilon_e + \frac{w_e^2}{2}\right) + e_r\right] + \frac{1}{r^2}\frac{\partial}{\partial r}\left\{r^2\left[\rho_e w_e\left(\varepsilon_e + \frac{w_e^2}{2}\right) + e_r + w_e(p_e + p_r) + q_e + S_r\right]\right\} = q_{ie} + f_{ie} w_e + \Psi_{ie}\left(E_{e(ie)} + \tfrac{1}{2} m_e w_e^2\right), \tag{57}$$

where ρ_e is the density of an electron gas ($\rho = \rho_i + \rho_e, \rho_e \ll \rho_i$), determined by number density of the electrons, n_e, and mass of an electron, m_e; f_{ie} is an interaction force between the ions and electrons per unit volume. This force tries to make the velocities of the ions and electrons equal ($w_i = w_e = w$). In addition q_{ie} is the thermal flux from the ions to electrons; Ψ_{ie} is a number intensity of electrons ripped from the ions per unit time and unit volume; $E_{e(ie)}$ is an internal energy of an electron just ripped off an ion.

It is logical to assume that an electron just ripped off of an ion has the same averaged thermal velocity as the ion ($v_e^2 \approx v_i^2$). Because of the relatively small electron mass compared to the mass of the ion, these electrons possess a kinetic energy corresponding to a temperature that is much lower than that of the ions. That is,

$$E_{e(ie)} = \frac{3}{2} k^{(B)} T_{e(ie)} \approx \frac{m_e v_e^2}{2} \ll \frac{m_i v_i^2}{2} = \frac{3}{2} k^{(B)} T_i, \tag{58}$$

$$\text{thus } T_{e(ie)} \approx \frac{m_e}{m_i} T_i \ll T_i.$$

Substituting f_{ie} from (56) into (57) and taking into account the mass conservation equation (55), one obtains the following equation for the internal energy of the electrons coupled with the energy density of radiation:

$$\frac{\partial}{\partial t}(\rho \varepsilon_e + e_r) = -\frac{1}{r^2}\frac{\partial}{\partial r}\left\{r^2\left[\rho w \varepsilon_e + e_r + q_e + S_r\right]\right\} - (p_e + p_r)\frac{1}{r^2}\frac{\partial}{\partial r}(r^2 w) + q_{ie} + \Psi_{ie} E_{e(ie)}. \tag{59}$$

Thus, to model two-component, two-temperature plasma dynamics in general, one must solve the set of equations (53)–(55) and (59) together with respective coupling equations for $p_i, p_e, p_r, \varepsilon_i, \varepsilon_r, e_r, q_i, q_e, S_r, q_{ie}, \Psi_{ie}$. However, in case of a violent bubble implosion (i.e., during typical bubble fusion experiments) the complete problem may be substantially simplified, and reduced to Eqs. (50)–(52) (see Appendices E–G). In the following subsections we discuss the reasons why and some details of the plasma model used in this study.

B. Kinetics of dissociation, ionizations, and nuclear reaction

All levels of dissociation and ionization were determined by linear kinetic equations[65] with the temperature, T, relative to the characteristic temperatures for dissociation T_d or ionization, T_k, with relaxation times, τ_k:

$$\frac{\mathrm{d}x_k}{\mathrm{d}t} = x_{k*}\frac{T - T_k}{T_k}\frac{1}{\tau_k}; \quad x_{k*} = x_{k-1}, \quad \text{if } T \geq T_k; \qquad x_{k*} = x_k, \quad \text{if } T < T_k, \tag{60}$$

$$(0 \leq x_k \leq 1, \quad k = d, d0, 1, 2, \ldots, Z, \quad d - 1 \rightarrow m).$$

The relaxation times τ_k were varied in the range $\tau_k = 1$ ps–5 ns. The first was close to the equilibrium state; the last corresponded to a frozen k reaction, because the total duration of the high temperature state was only about 2 ns (see Sec. IX).

In order to estimate the production of fusion neutrons, the neutron kinetics model given by Gross[66] and by Duderstadt and Moses[53] was used in conjunction with the local, instantaneous HYDRO code evaluations during the bubble implosion process:

$$J_n = J_T = \tfrac{1}{2}\langle \sigma v \rangle (n_D)^2, \tag{61}$$

where J_n and J_T are numbers of D/D fusion neutrons and tritium (T) produced per unit time and unit volume, respectively, n_D is the concentration of the deuterons per volume unit, and $\langle \sigma v \rangle$ is the weighted cross section for the fusion reaction (Bosch and Hale,[67] Duderstadt and Moses[53]). The

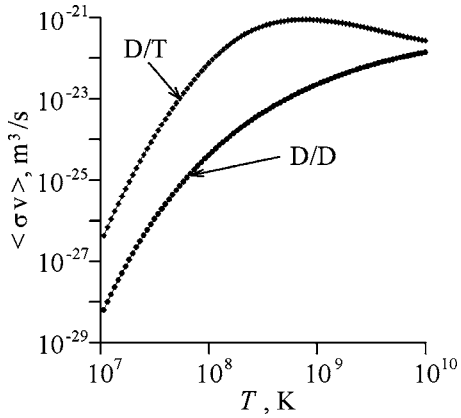

FIG. 5. The dependence of the weighted nuclear cross section, $\langle \sigma v \rangle$, for D/D and D/T fusion reactions vs temperature (Ref. 67).

temperature dependence of $\langle \sigma v \rangle$ is shown in Fig. 5 for D/D and T/D reactions. It is seen that T/D fusion is more than 10^2 times more intensive than D/D fusion at 10^8 K.

The concentration of deuterons, n_D, is determined by the density and by number of acetone molecules per unit mass, $N^{(A)}/M$. As each D-acetone (C_3D_6O) molecule has six deuterons one may write

$$n_D = \frac{6\rho N^{(A)}}{M} = 0.56 \times 10^{26}\rho. \tag{62}$$

The number of D/D thermonuclear neutrons or tritium nucleus produced per implosion or period of the acoustic field may be calculated by integration of the volume of the bubble and by the time during the period, $2\pi/\omega$, of the acoustic field:

$$N = \int_0^{2\pi/\omega} dt \int_0^a 4\pi r^2 J_n dr = \int_0^a N_r dr,$$
$$N_r(r) = 4\pi r^2 \int_0^{2\pi/\omega} J_n dt, \tag{63}$$

where $N_r(r)$ is the distribution function of neutron production in the bubble. Thus the evolution in time of neutron (and tritium) production in an imploding bubble is

$$N(t) = \int_0^t dt \int_0^a 4\pi r^2 J_n dr. \tag{64}$$

VIII. NUMERICAL METHOD

All equations for low or high Mach number were implemented in a "liquid drop" scheme, which has been successfully used in many prior studies of collapsing bubbles (Nigmatulin *et al.*,[14,35] Akhatov *et al.*[68]). According to this scheme the entire region was divided into three zones, namely

(1) $0 \leqslant r \leqslant a(t)$—the gas/vapor zone in the bubble, where the equations of state of the gas/vapor are used and the thermal conductivity is $\lambda = \lambda_G$.

(2) $a(t) \leqslant r \leqslant B(t)$—the compressible liquid "drop" zone just outside of the bubble, where the equations of state of the liquid are used and the thermal conductivity is $\lambda = \lambda_L$. In this zone a variation of pressure with time and space may be high enough for compressibility of the liquid to be essential. The external radius, $B(t)$, of this zone is several bubble radii in size but is much smaller than the characteristic size of the acoustic chamber.

(3) $B(t) < r < \infty$—the liquid zone between the compressible liquid drop and the acoustic chamber wall. The external radius of the liquid drop boundary, B, is chosen large enough so that the velocity of the liquid on the boundary, $w_B(t) = dB/dt$, is small with respect to the liquid speed of sound, and the variation of pressure is small, so the liquid may be treated as incompressible even for the high Mach number stage in the vapor or in the liquid near the bubble.

The dynamics of $B(t)$ can be described by a generalized Rayleigh-Plesset equation (44):

$$B\frac{dw_B}{dt} + \frac{3}{2}w_B^2 = \frac{p_B - p_I}{\rho_{L0}} + \frac{B}{\rho_{L0}C_{L0}}\frac{d}{dt}(p_B - p_I), \quad w_B = \frac{dB}{dt}, \tag{65}$$

and detailed numerical calculations of the so-called gas dynamic equations (50)–(52) for a compressible fluid is needed only in zones (1) and (2).

To make the calculations for the low Mach number stage (Sec. V) the Dorman–Prince numerical method (Hairer, Norsett, and Wanner[69]) was used to solve the generalized Rayleigh-Plesset equations (44) and (65) for bubble radius, $a(t)$, and liquid drop radius, $B(t)$. During vapor bubble growth up the point where it reaches a maximum radius, we used 200 equally sized grids in the gas zone $[0 \leqslant r \leqslant a(t)]$ and 200 cells in the liquid "drop" zone $[a(t) \leqslant r \leqslant B(t)]$, which were increased geometrically in size. The ratio of the boundary cells sizes in the gas and liquid was

$$\frac{\Delta r_G}{\Delta r_L} = \sqrt{\frac{D_G}{D_L}} \quad \left(D_k = \frac{\lambda_k}{\rho_k c_k}, k = L, G\right), \tag{66}$$

where D_k is the thermal diffusivity of the gas ($k=G$) and liquid ($k=L$).

During bubble growth the temperature gradient in the vapor is much smaller than in the liquid because $D_L \ll D_G$, and the thermal wave penetrates in the liquid much more slowly than in the gas. When the bubble begins to contract the thermal boundary layer in the vapor and liquid becomes very thin due to extremely rapid growth of the pressure in the bubble that determines the temperature on the interface, which is close to $T_S(p)$ (see Sec. XI). To control accuracy we have to use a finer grid near the bubble interface, $r = a(t)$. Therefore in calculations the current solution at the beginning of fast bubble collapse, the boundary layers were interpolated onto 1000 nodes in the gas and 1000 nodes in the liquid that increase geometrically in size from $\Delta r_G = a/2000$ at the interface. The ratio (66) for Δr_G and Δr_L near the interface stayed unchanged.

When the Mach number, $M=|w_{La}|/C_G$, reached 0.05–0.2, the gas dynamics model (50)–(52), with the compression and shock waves was initialized and used. The Godunov numerical method (Godunov *et al.*[70]), with first-order accuracy in time and in space, was used. This method is based on the exact solution of the Riemann problem. The final calculations were carried out in mixed Eulerian and Lagrangian coordinates (Topolnikov[71]).

IX. CAVITATION BUBBLE CLUSTER DYNAMICS IN AN ACOUSTIC FIELD

In the experiments of Taleyarkhan *et al.*[1,2] the acoustic field acted on a cluster of bubbles consisting of ~1000 bubbles. The maximum radius of the bubble cluster was about $R\approx 4$ mm. The measured pressure amplitude of the acoustic field ($\Delta p=15$ bars) in the acoustic antinode was the incident pressure on the periphery of the bubble cluster. This was not the same as the pressure on the bubbles near the center of the cluster. The bubbles in the central region of the cluster may be subjected to a much higher compression pressure than the peripheral bubbles because of multibubble dynamics. These dynamics induces an amplification of the compression wave (Nigmatulin[33]). For a spherical bubble cluster the focusing and intensification of compression waves was investigated numerically by Wang and Brennen,[72] by Matsumoto,[73] by Shimada, Matsumoto, and Kobayashi,[74] and by Kedrinsky.[75] The two-dimensional amplification of compression waves in bubbly liquids was also investigated by Nigmatulin *et al.*[76]

Let us consider a spherical bubble cluster comprised of spherical bubbles, which is surrounded by a noncompressible liquid subjected to harmonic incident pressure oscillations in a standing acoustic wave field ($\Delta p=15$ bars). First, the low Mach number stage when the kinetic energy of the liquid is accumulated will be considered. The center of the cluster is placed at the origin of a spherical Lagrangian coordinate system (r',t), where the partial derivative $\partial/\partial t$ corresponds to the material derivative, $\mathrm{d}/\mathrm{d}t$, for Eulerian coordinates. It is necessary to distinguish the radial coordinates: r is the radial coordinate (i.e., the microcoordinate) inside the spherical bubble, which is used in Secs. V–VIII, XI, and XII while r' is the radial coordinate (i.e., the macrocoordinate) in the two-phase cluster that is used in Sec. IX; in particular in Eqs. (67) and Fig. 6.

The cluster may be considered as two fluid continua with two pressures (Nigmatulin,[33] Brennen,[77] Matsumoto,[73] Kedrinskiy[75]). The first one is an averaged, or macroscopic, pressure in the liquid, p, which can be identified as the incident pressure around the bubble. The second one is the pressure in the bubbles, p_G. The set of equations for bubbly liquid motion is (Nigmatulin[33])

$$\frac{\partial x}{\partial t}=v,\quad \frac{\partial v}{\partial t}=\frac{1}{\rho_0}\left(\frac{x}{r'}\right)^2\frac{\partial p}{\partial r'},$$

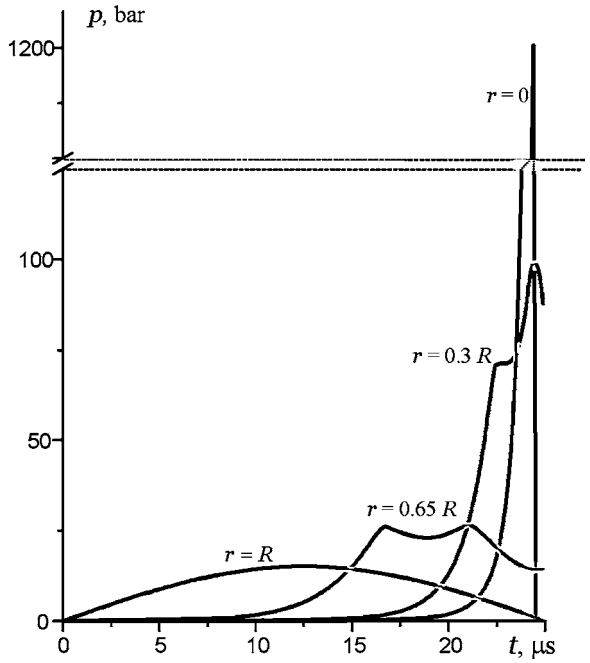

FIG. 6. The evolution of liquid pressure intensification within an imploding bubble cluster at different radii, r (shown by the corresponding labels), for a cluster with 1000 bubbles ($a_0=300$ μm, $\alpha_{G0}=0.042$) subjected to a 15 bar compression pressure on the boundary of the bubble cluster ($r=R$).

$$\begin{gathered}
\left(1-\phi^{(1)}\right)a\frac{\partial w_{La}}{\partial t}+\left(1-\phi^{(2)}\right)1.5w_{La}^2 \\
=\frac{p_{La}-p}{\rho_{L0}}+\frac{a}{\rho_{L0}C_L}\frac{\partial}{\partial t}(p_{La}-p), \\
\frac{\partial a}{\partial t}=w_{La}+\frac{j}{\rho_L}\approx w_{La},\quad p_{La}=p_G-\frac{2\sigma}{a}-\frac{4\mu_L w_{La}}{a}, \\
p_G=p_{G0}\left(\frac{a}{a_0}\right)^{-3\kappa}, \\
\alpha_G=\frac{\alpha_{G0}a^3}{(1-\alpha_{G0})a_0^3+\alpha_{G0}a^3},\quad p_L=\rho_{L0}+C_L^2(\rho_L-\rho_{L0}), \\
\rho_0=\rho_{L0}(1-\alpha_{G0}).
\end{gathered} \tag{67}$$

Here $x(r',t)$ and $v(r',t)$ are the Eulerian radial coordinate and radial velocity of the two-phase fluid (mixture of the liquid and bubbles), α_G is the volume (void) fraction of the bubbles, $\phi^{(1)}=1.1\alpha_G^{1/3}$ and $\phi^{(2)}=1.5\alpha_G^{1/3}$ are the "collectiveness" coefficients due to the finite volume of the liquid corresponding to a single bubble; subscript 0 corresponds to the initial state. The polytropic coefficient, κ, was taken to approximate the evolution of p_G calculated by more precise codes (i.e., $\kappa=1.0$ for slow expansion and $\kappa=1.32$ for compression of the bubbles).

Numerical calculations were made when the cluster ($R_0=4$ mm) was initially uniform with $\alpha_{G0}=0.04$ corresponding to 1000 bubbles with radius $a_0=300$ μm. Then on the boundary of the bubble cluster $[r'=R(t)]$ the pressure, $p(t)$, corresponded to the compression part of a sinusoidal

excitation with amplitude 15 bars. A compression wave propagated to the center of the cluster initiating compression of the bubbles. The compression wave was led by an elastic precursor with sound speed C_L in pure liquid. Then the main wave followed initiating the collapse of the bubbles. In Fig. 6 the evolution of liquid pressure, $p(t)$, at four points within the cluster: $r'=R$, $0.65R$, $0.33R$, and 0. It is seen that the reflection of the waves from the center of the cluster, where $v=0$, produces very strong amplification of the pressure and concentrates it over a short period of time.

Using the averaged incident pressure evolution, $p_I = p(r',t)$, and the equations in Sec. V we can make a second approximation by calculating the process in the bubble (i.e., using radial coordinate r) and considering it as a test bubble at different radial positions within the cluster, r'. Naturally, the most interesting calculations are the calculations for the central zone of the cluster ($r' < 0.2\ R$), where the bubbles experience the most intensive compression.

X. COALESCENCE

Investigation of the incident pressure evolution in bubble clusters (Sec. IX) being forced by the acoustic pressure field shows that the pressure rarefaction within the cluster is smaller than the incident acoustic pressure, −15 bars, but the compression impact of the incident pressure is much higher and of shorter duration than the incident acoustic pressure, +15 bars (see Fig. 6). During rarefaction the maximum bubble radius in the cluster reaches only 100–300 μm, which is too small to have an effective cumulation of the compression wave in the bubble and thus does not produce a thermonuclear central core in the imploded interior bubbles. Nevertheless, there should be larger bubbles in the cluster.

One of the main mechanisms leading to larger bubble sizes is coalescence of bubbles. Let us estimate the time, which is needed for bubbles to coalesce. The bubble coalescence process within the expanding bubble clusters is mainly controlled by liquid film drainage dynamics between adjacent bubbles. Eventually the film drainage is driven by surface tension forces and is limited by liquid inertia. The surface tension pressure driving film drainage can be estimated as

$$\Delta p_\sigma \sim \sigma / R_f. \tag{68}$$

Here R_f is a liquid film mean radius of the curvature, which is related to a bubble radius as $R_f \sim \varepsilon_f a$, where ε_f is a dimensionless parameter characterizing the shape of the liquid film. The respective surface tension force acting on the interbubble liquid film is then

$$F_\sigma \sim R_f^2 \Delta p_\sigma, \tag{69}$$

where the factor R_f^2 is proportional to the characteristic area of liquid film drainage. Also, the mass of liquid draining between the bubbles can be estimated to be

$$m_f \sim \rho_L R_f^3, \tag{70}$$

Thus the acceleration of the draining liquid film is

$$\dot{w}_f \sim \frac{F_\sigma}{m_f} \sim \frac{\sigma}{\rho_L R_f^2}. \tag{71}$$

Therefore the time that is needed for the liquid film to drain sufficiently to have bubble coalescence is

$$t_f \sim \sqrt{\frac{a}{\dot{w}_f}} \sim \sqrt{\frac{\rho_L}{\sigma} \varepsilon_f^2 a^3}. \tag{72}$$

Since $\rho_L/\sigma \approx 3\times 10^4\ \mathrm{s^2/m^3}$, $a \approx 100\ \mu$, and $\varepsilon_f \sim 10^{-2}$ we have $t_f \sim 2\ \mu$s. That implies that bubbles within an expanding bubble cluster have sufficient time to coalesce.

In addition, liquid film evaporation during bubble cluster expansion will further thin the liquid film and thus promote bubble coalescence. However, evaporation is not very important in reducing the liquid film thickness because of the large difference between the liquid and vapor densities ($\rho_L/\rho_G \sim 10^4$) for the rarefaction conditions during bubble growth.

It was estimated that during the growth phase of the bubble cluster, about 10–20 bubbles coalesce forming larger interior bubbles of radius 600–800 μm. This size bubble provides effective focusing of the subsequent shock waves leading to thermonuclear conditions in the central region of the imploding bubbles. If there were initially 10^3 bubbles in the cluster, after coalescence we would have 50–100 larger bubbles, some of which would be compressed by the liquid pressure transient within the cluster shown in Fig. 6.

It should be noted that the analysis on liquid pressure intensification discussed in Sec. IX implicitly assumes that the bubbles within a bubble cluster remain spherical during an implosion. Sometimes this may not be true (Margulis and Margulis[78]), however, details of the bubble interactions are not yet available. Nevertheless, the effect of bubble distortion may not be too large. In particular, the wavelength, Λ, of the initial disturbances to the spherical shape of the large bubbles due to the coalescence of smaller bubbles, is on the order of $2R_f$ (i.e., these disturbances are relatively short wave disturbances, $\Lambda \sim 2R_f \ll 2a$). These disturbances do not grow much because of action of the liquid viscosity and surface tension (Aganin *et al.*[79]). Thus the spherical shape of the bubble during implosions remains if the initial value of the perturbation, δa°, of the long wave ($\Lambda \sim 2a$) disturbance of the spherical shape is small enough:[79]

$$\delta a^\circ / 2a \leqslant 10^{-2}. \tag{73}$$

XI. RESULTS

To simulate the ORNL experiments let us consider a single cycle of the vapor bubble dynamics in D-acetone under the influence of a periodic acoustic field. The impressed pressure is given by

$$p_I = p_0 + \Delta p_1 \sin(2\pi\omega t), \quad p_0 = 1\ \text{bar}, \quad \Delta p_1 = 15\ \text{bars}, \tag{74}$$

which corresponds to the acoustic forcing in the ORNL experiments (Taleyarkhan *et al.*[1,2]).

Since Sec. VIII shows that the liquid pressure can strongly increase when the acoustic compression wave interacts with the bubble cluster, we have assumed two compres-

sion laws. The first one is that the incident pressure, p_I, for the bubble under consideration in the central region of the cluster varies according to the same sinusoidal form as in (74) but with a higher amplitude, $\Delta p_2 = 50$ bars, during the compression period.

The second compression law used the pressure intensification shown in Fig. 6. This compression of the bubbles ($a_{\max} = 600-800\ \mu$m) is much shorter ($\Delta t \approx 1-5\ \mu$s) but much stronger ($\Delta p \approx 100-1200$ bars) than that of the 15 bar incident pressure on the outer part of the bubble cluster. Significantly, both compression laws give similar results (i.e., $\Delta p_2 = 50$ bars was chosen to produce similar results), that is, the creation of thermonuclear conditions within the imploded bubbles.

We assumed that at the initial moment ($t=0$) the vapor in the bubble and the liquid around the bubble are at rest and there was thermodynamic equilibrium:

$$p_0 = 1 \text{ bar}, \quad T_0 = 273 \text{ K}[p_S(273 \text{ K}) = 0.087 \text{ bar}],$$
$$\omega = 19.3 \text{ kHz}, \tag{75}$$

$$t = 0: \quad a_0 = 0.4 - 10\ \mu\text{m}, \quad w_G(r,0) = w_L(r,0) > 0, \tag{76}$$
$$p_G(r,0) = p_S(T_0), \quad T_G(r,0) = T_L(r,0) = T_0.$$

These conditions correspond to the initial pressure jump at the bubble interface that initiates expansion of the bubble and evaporation at the interface when the incident pressure in the liquid becomes less than at the interface [see (44) and (46)],

$$p_I < p_{La} = p_G - \frac{2\sigma}{a}. \tag{77}$$

The initial data are important only at the beginning of the bubble growth period (i.e., during the time interval of about 1 μs). The calculations showed that the bubble dynamics is not sensitive to variation of a_0, T_G and other parameters at later times.

Figure 7 presents the time evolution of the bubble's radius, a, interface velocity, $\mathrm{d}a/\mathrm{d}t \approx w_{La}$, vapor mass, m_G, intensity of the evaporation ($j>0$) or condensation ($j<0$), uniform pressure in the bubble, p_G, and density $\rho_G(r=0)$ and temperature $T_G(r=0)$ at the center of the bubble for a single cycle of bubble growth and collapse during the low Mach number stage (see Sec. V).

Figure 8 presents the time evolution of the bubble radius, a, wall velocity, $w_{La} \approx \mathrm{d}a/\mathrm{d}t$, pressure, p_{La}, density, ρ_{La}, and temperature, T_{La}, on the interface ($r=a$) during the final stage of bubble implosion at high Mach number.

The points 1–26 marked on the curves $a(t)$ in Figs. 7 and 8 denote times during the bubble dynamics process. For these times the spatial distributions of the pressure, temperature, density, and radial velocity are shown in Figs. 9–13. The transition from the "slow" (low Mach number) homobaric model to the "fast" (high Mach number) shock wave model was made at time t_7 when there are homobaric conditions in the bubble and negligibly small changes of the liquid

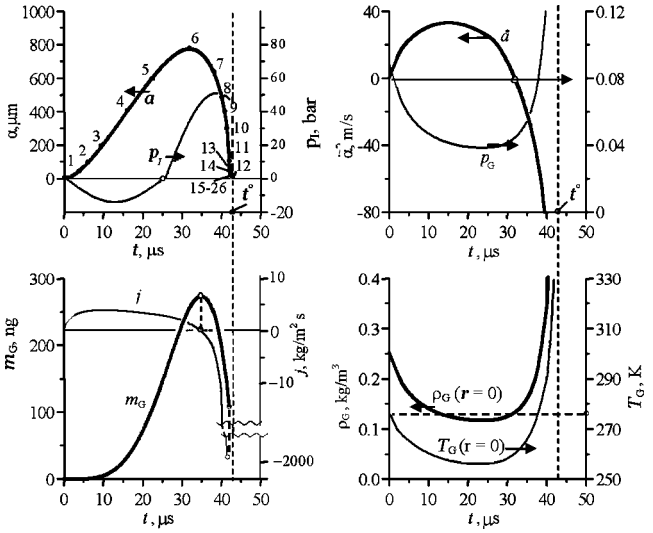

FIG. 7. The vapor bubble parameters as functions of time for the low Mach number (microsecond) stage. Numbers correspond to times, t_n ($n=1, 2, \ldots, 26$), for which the spatial distributions of the parameters are given in Figs. 9–13.

density (i.e., at $\mathrm{M} \sim 0.1-0.2$). Slight variations of the time of transition do not have a strong influence on the subsequent bubble dynamics.

The maximum values of the velocity, pressure, temperature, and density of the liquid are on the interface, and they reach $w_{La} \approx 2$ km/s, $p_{La} \approx 0.5$ Mbar, $T_{La} \approx 2500$ K, $\rho_{La} \approx 2200\ \text{kg/m}^3 \approx 2.5\ \rho_{L0}$. The duration around this state at the interface is $\sim 5-10$ ns.

It is seen that the time of the bubble growth is nearly three times longer than for the bubble collapse.

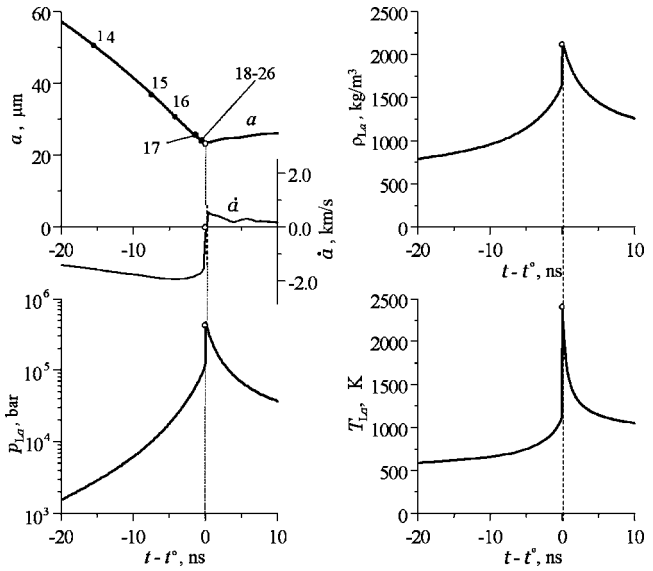

FIG. 8. Evolutions of the bubble radius, interface velocity and liquid parameters at the interface during the final nanosecond (i.e., high Mach number) stage of bubble implosion ($t^\circ = 41.9932\ \mu$s is the time corresponding to the minimum bubble radius). Numbers correspond to times, t_n ($n=14, 15, \ldots, 26$), for which the spatial distributions of these parameters are given in Figs. 10–13.

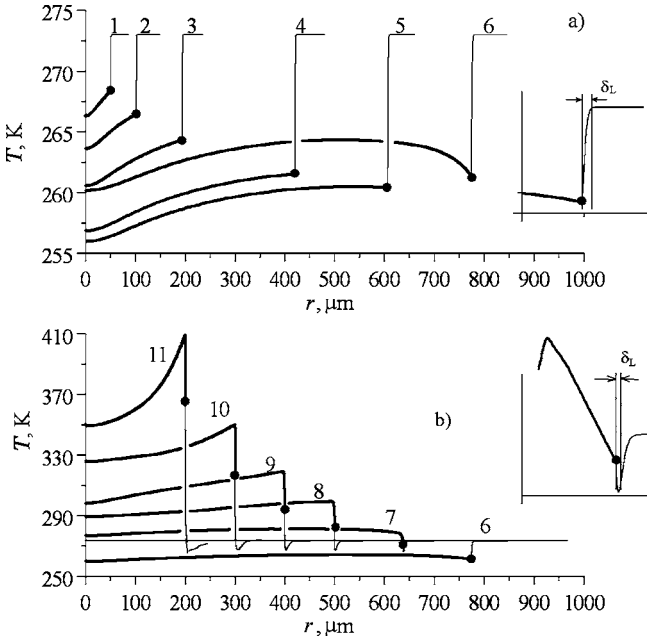

FIG. 9. Temperature profiles in the vapor and liquid during expansion phase, (a), and the initial contraction phase, (b), of the bubble dynamics during the microsecond (i.e., low Mach number) stage and transition to the high Mach number stage. The numbers denote times: t_1=4.17 μs, t_2 =6.37 μs, t_3=9.64 μs, t_4=16.6 μs, t_5=22.6 μs, t_6=31.9 μs, t_7=38.0 μs, t_8=39.9 μs, t_9=40.8 μs, t_{10}=41.4 μs, t_{11}=41.7 μs. The solid dots on the curves correspond to the interface, the solid and thin lines correspond to the vapor and liquid, respectively.

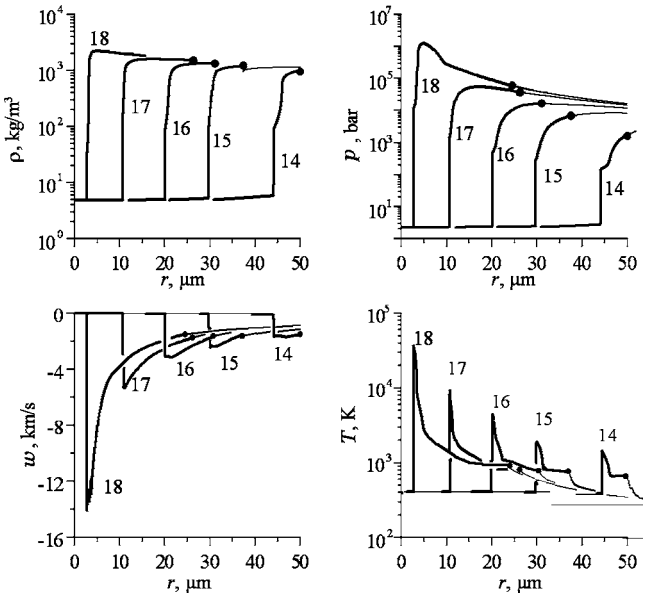

FIG. 11. Spatial profiles of the vapor and liquid parameters during shock wave convergence (the nanosecond, high Mach number, stage). The numbers denote times: $t_{14}=t^*-15$ ns, $t_{15}=t^*-7.5$ ns, $t_{16}=t^*-4.1$ ns, $t_{17}=t^*-1.9$ ns, $t_{18}=t^*-0.9$ ns, where $t^*\approx41.993$ ns is the time corresponding to the minimum bubble radius. The solid dots on the curves correspond to the interface, the solid and thin lines correspond to the vapor and liquid, respectively.

Temperature distributions during bubble expansion and early contraction (the microsecond stage) in Fig. 9 are characterized by a very thin temperature boundary layer in the liquid near the interface due to a rapid drop of the temperature on the interface during expansion of the vapor. This temperature drop changes into to an extremely fast temperature increase on the interface during bubble implosion that is induced by the compression of the vapor. The thickness of this boundary layer may be estimated by $\delta_L\sim\sqrt{D_L t}(D_L$

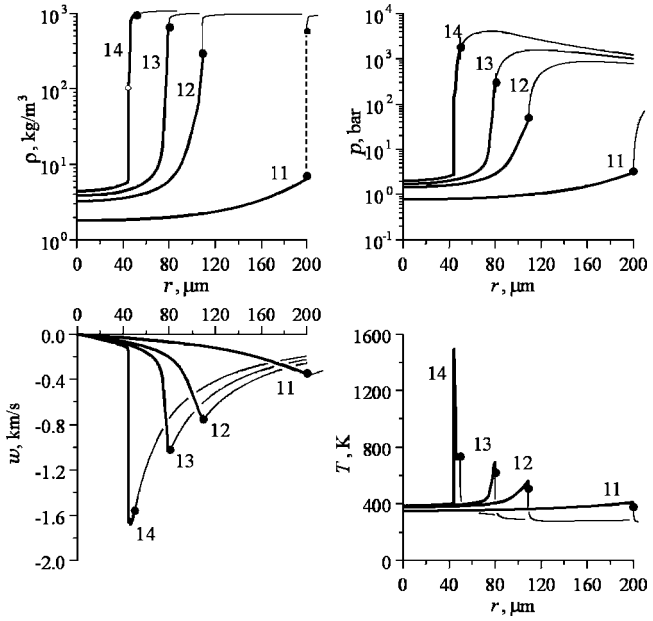

FIG. 10. Spatial distributions of the vapor and liquid parameters during a latter stage of bubble implosion (i.e., the submicrosecond, high Mach number, stage). The numbers denote times: $t_{11}=t^*-0.25$ μs, $t_{12}=t^*-0.07$ μs, $t_{13}=t^*-0.04$ μs, $t_{14}=t^*-0.015$ μs, where $t^*\approx41.993$ μs is the time moment corresponding to the minimum bubble radius. The solid dots on the curves correspond to the interface, the solid and thin lines correspond to the vapor and liquid, respectively. The open circle denotes the thermodynamic critical condition.

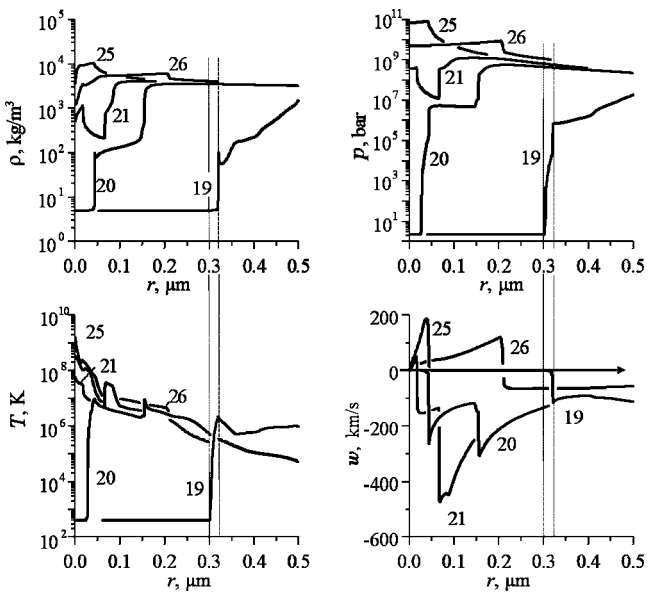

FIG. 12. The vapor parameters distributions in the bubble's center region corresponding to focusing and reflection of the shock and continuous compression waves (the picosecond, high Mach number, stage). The dotted and dashed lines indicate the positions of thermal wave and isothermal shock wave fronts, respectively, at $t=t_{19}$. The numbers mark the times: $t_{19}=t^*-2.0$ ps, $t_{20}=t^*-0.29$ ps, $t_{21}=t^*-0.11$ ps, $t_{25}=t^*$, $t_{26}=t^*+0.17$ ps, where $t^*=t^*-782.33$ ps is the time when the maximum temperature at $r=r^*=27$ nm takes place.

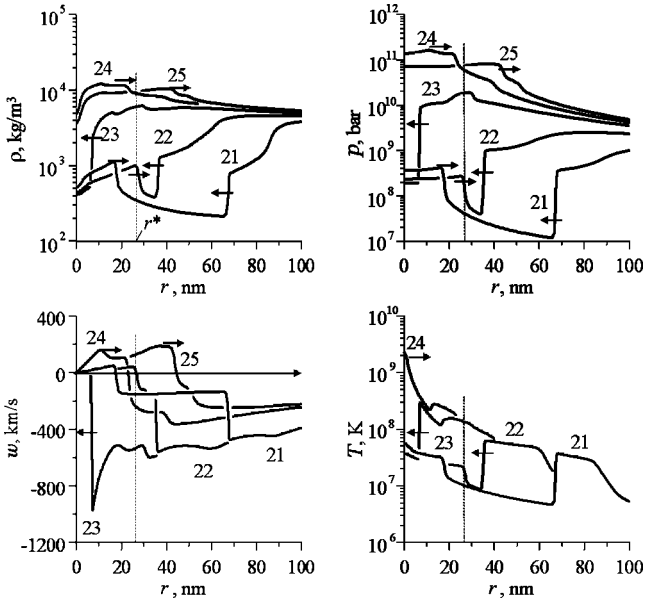

FIG. 13. The final stage of bubble implosion. The vapor parameters distributions near the bubble's center between two interacting shock waves (subpicosecond, high Mach number, stage). The dashed line indicates the radial position of the maximum neutron production point r^*. The numbers denote times: $t_{21}=t^*-0.11$ ps, $t_{22}=t^*-0.06$ ps, $t_{23}=t^*-0.02$ ps, $t_{24}=t^*-0.01$ ps, where $t_{25}=t^*$.

$\approx 0.13\times 10^{-6}$ m^2/s). The drop of the temperature on the interface $[T_a \approx T_S(p)]$ because of bubble expansion takes place until $t\approx 30$ μs [Fig. 9(a)], which gives $\delta_L \approx 2$ μm. But the divergent flow of the noncompressible liquid [when $a(t)$ is growing] makes it even thinner (i.e., proportional to a^{-2})[33–35,80]

$$\delta_L \sim \left(\frac{a(t)}{a_0}\right)^{-2}\sqrt{D_L t}. \tag{78}$$

That is why the temperature profile in the liquid looks like a jump next to the interface. The bubble collapses after t_7 [Fig. 9(b)] and the interface temperature, T_a, increases rapidly (during only 4 μs). The thermal boundary layer, with liquid temperature falling from the interface, would be about three times thinner, but the spherically convergent flow [when $a(t)$ is getting smaller] makes it thicker proportional to a^{-2} [see $T(r)$ in Figs. 9(b) and 11].

The thickness of the temperature boundary layer in the compressible vapor is $\delta_G \sim \sqrt{D_G t}$ ($D_G \approx 53\times 10^{-6}$ m^2/s), and during the expansion phase (i.e., until $t\approx 30$ μs) the thickness of the temperature boundary layer when the temperature in the vapor falls from the interface to the center of the bubble [see the temperature distributions for t_1-t_6 in Fig. 9(a)] is much thicker: $\delta_G \sim 40$ μm. However, the fast contraction of the vapor with the growth of the temperature takes place during $t\sim 1$ μs, and the thickness of the boundary layer in the gas with the temperature falling to the interface [see temperature distributions for t_8-t_{11} in Fig. 9(b)] becomes very thin as in the liquid: $\delta_G \sim 7$ μm. Then nonuniform profiles of temperature in the gas and in liquid are formed.

A critical point at the interface takes place at the moment that is close to t_{12} ($t_{12}=t^\circ-70$ ns, see Fig. 10), when radius of the bubble $a\approx 110$ μm, velocity of the interface, $w_{La}=w_{Ga}\approx -800$ m/s, and pressure in the bubble is no longer uniform, but there is not yet a shock. At this moment condensation stops because the liquid and vapor on the interface becomes a supercritical fluid ($p\geqslant p_{cr}=46$ bars, $T\geqslant T_{cr}=508$ K), and there is no longer any difference between vapor and liquid.

It is interesting that around this moment ($t\approx t_{12}$) the pressure distribution in the liquid is smooth (Fig. 10), but the density distribution looks like a jump near the interface where this density increases three times, however, it is not a jump. The sharp increase of the density follows the sharp drop of the liquid temperature in the thermal boundary layer.

During the subcritical phase of the bubble implosion more than half of the evaporated vapor mass ($m_G \approx 260$ ng) condenses. The final mass of vapor ($m_G \approx 100$ ng) after the transition to a supercritical fluid remains constant and the bubble keeps on contracting from $a\approx 110$ μm to the minimum bubble radius $a_{min}\approx 24$ μm (see Fig. 8), as compared to a minimum radius of 0.3–1 μm in typical SBSL experiments (Moss *et al.*[21–23]). Significantly, the mass of the highly compressed gas (vapor) in bubble fusion experiments is 10^5–10^6 times larger than in typical SBSL experiments, thus there is more material available to undergo fusion reactions.

The formation of a strong compression wave transforming to a strong shock wave is shown in Figs. 10 and 11. This stage is short and takes less than 0.5 μs after t_{10}. At moment t_{11} the pressure distribution is nonuniform (i.e., the homobaric assumption is no longer valid) and intensive continuous compression occurs when the pressure at the interface ($r=a$) is 3.7 times larger than at the center of the bubble ($r=0$). At moment t_{14} the formation of a strong shock [i.e., pressure jump ($r\approx 40$ μm)] takes place (see the transparent circle in Fig. 10).

A continuous and relatively smooth increase of the pressure at the bubble's interface has great advantages compared with the compression in typical "laser-induced fusion" experiments, where there is a much faster increase of the pressure. A smooth increase of the pressure leads to a continuous (close to isentropic) compression and a shock wave that is initiated close to the center of the bubble ($r\approx 40$ μm $\ll r_{max}=800$ μm, see Fig. 10).

The intensity of the shock (i.e., the pressure, temperature, and velocity after the shock) increases on converging to the center of the bubble, but the ratio of the density after the shock (ρ_+) to the density before the shock (ρ_-) tends to a maximum value (Landau and Lifshitz,[51] Rakhmatulin,[52] Sedov[58]), which for a molecular gas with a low adiabatic exponent of $\gamma_m=1.125$ is

$$\frac{\rho_+}{\rho_-}\to\left(\frac{\rho_+}{\rho_-}\right)_{max}=\frac{\gamma_m+1}{\gamma_m-1}=17.0. \tag{79}$$

In comparison, the maximum values of compression on the shock wave (ρ_+/ρ_-) for monatomic ($\gamma_m=5/3$) and diatomic gas ($\gamma_m=7/5$) are much less and equal to 4 and 6, respectively.

After the shock a continuous compression wave follows to the center of the bubble (see the distributions for $t_{14}-t_{20}$ in Figs. 11 and 12. The compression shock wave with the trailing continuous compression wave qualitatively corresponds to the self-similar solutions for the spherically symmetrical flow of a perfect gas converging to the origin from infinity (Guderley,[81] Chernousko,[82] Nigmatulin,[83] Zababakhin and Zababakhin[84]) with a leading shock wave. These theoretical solutions give the intensity of a converging shock wave with the pressure and temperature tending to infinity at the moment of the reflection from the center. However, dissipation processes due to viscosity, dissociation, ionization, photon emissions, and thermal conductivity effectively mitigate the compression process so that the pressure and temperature remain finite. Lin and Szeri[85] demonstrated this for SBSL.

As can be seen in Fig. 12, the leading shock compression wave is focusing and approaching the bubble's center at time moment t_{20}, and a trailing compression wave, which is much stronger, reaches and reflects from the center at time t_{24}. The simulation shows that the maximum neutron production is produced during the reflections of these waves from the center and interaction with each other. A detailed picture of the interaction of these two waves is shown in Fig. 13.

A thermal precursor is formed before the shock because of the increased thermal conductivity with temperature [in our model, (43), the thermal conductivity varied as $T^{1/2}$] and it becomes important near the bubble's center when the shock-induced temperature is higher than 10^6 K. This precursor is due to the variable thermal conductivity and it increases the temperature and pressure (see the dotted vertical lines and plots for T_G, ρ_G, p_G, and w_G in Fig. 12 at time t_{19}) but does not cause much fluid displacement ($w \approx 0$) or change of density. In contrast, arrival of the shock (see the dashed vertical lines in the plots for t_{19}) initiates a high-speed flow ($w > 10^5$ m/s). As a result the thermal precursor smears the shock wave front somewhat when the pressure and temperature fronts are ahead of the density and velocity shock, which is called an "isothermal jump" (Zeldovich and Raiser,[44] Landau and Lifshitz,[51] Belokogne,[86] Zababakhin and Simonenko[87]) and is marked by the dashed vertical lines in Fig. 12. Nevertheless, because of the shortness of the time scales for the transient of interest, the modeling of thermal conductivity (and thus heat loss) does not appear to have a strong effect on the maximum temperatures and pressures.

Dissociation takes place during ~2 ns after t_{17} in the region $r < 1.5$ μm. As can be seen in Fig. 12 a highly compressed core with temperature $T > 10^7$ K is formed in the region $r < 200-250$ nm during ~0.3 ps (between t_{20} and t_{25}). During this high-temperature condition ionization takes place, and if the ionization relaxation times for the electrons at high temperatures ($T_k > 100$ eV $\approx 10^6$ K, see Appendix A) are small enough [$\tau_k < 0.1-0.2$ ps, see (60)], then the plasma in this hot core becomes fully ionized: $x_k = 1$, for all electrons ($k = 1, \ldots, 14$) during ~0.3 ps.

The state of the dense plasma with extremely high temperature, pressure, and density that can produce thermonuclear fusion ($T \sim 10^8$ K, $p \sim 10^{11}$ bars, $\rho \sim 10$ g/cm^3) takes place only in a very small central zone (the thermonuclear core), $r < 60-65$ nm (see Fig. 13), of the bubble

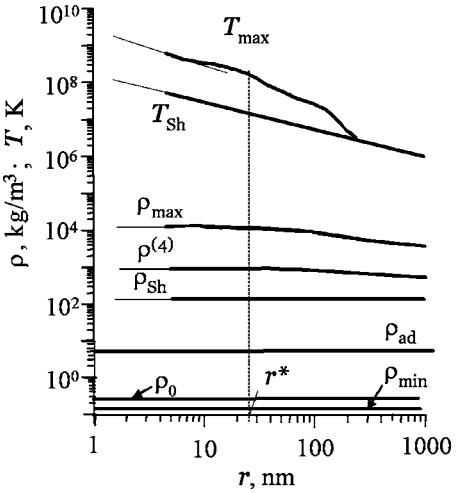

FIG. 14. The maximum vapor/plasma density, ρ_{max}, maximum temperature, T_{max}, the density ρ_{Sh}, and temperature, T_{Sh}, after the leading shock wave as functions of radial coordinate near the center of the bubble. The line labeled $\rho^{(4)}$ is the density after the continuous compression wave following after the leading shock wave. The horizontal lines labeled ρ_0, ρ_{min}, and ρ_{ad} correspond to the initial vapor density [see the line $\rho_G(r=0)$ on Fig. 7], densities after a continuous homobaric expansion (ρ_{min}) and practically isentropic (adiabatic) compression (ρ_{ad}).

when its radius is $a \approx 24$ μm. To resolve this very important but tiny region it was necessary to use a very fine computational grid in the central zone. In our calculations the distribution of the parameters at moment t_{12} was obtained with a 1000-cell grid. Then this distribution was interpolated on a 2000–cell grid with the same sizes of the grid for $r > 5$ μm and with much smaller size of the cell ($\Delta r = 0.1$ nm) near the center. Also the final calculations were done using Lagrangian coordinates to capture the steep shock wave fronts more accurately.[71]

Figure 14 displays the maximum values of vapor density and temperature near the bubble's center achieved during the implosion process, and Fig. 15 displays the radial distribution of the neutron production function N_r [see (63)]. Two solutions are shown in these figures: the first one accounts for vapor ionization and the second one assumes no absorp-

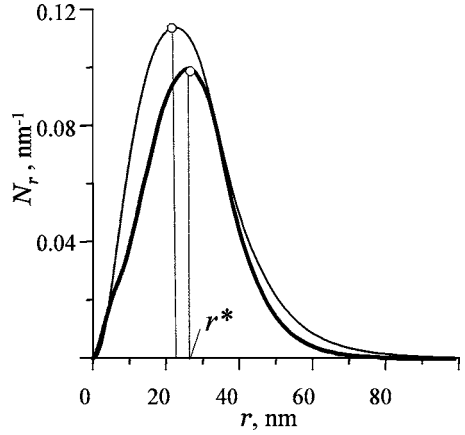

FIG. 15. The radial distribution of neutron output distribution, $N_r(r)$. The thick line depicts an ionized vapor and the thin line a nonionized vapor.

tion of thermal ionization. It can be seen that the effect of ionization is not great.

There is a radius, $r=r^*$, where the maximum neutron production, $N_r(r)$ (see Fig. 15), takes place. This maximum is explained by the interplay of two factors: closer to the center of the bubble the maximum temperature and density are larger (see Figs. 13 and 14), but there is much less material there and the time duration is shorter. This maximum corresponds to a radial coordinate r^*, which equals $r^*=27$ nm for an ionized vapor and $r^*=22$ nm for the hypothetical case without ionization.

The values of the parameters at the location of the maximum neutron production is marked by superscript *:

$$T^* = T(t,r^*), \quad p^* = p(t,r^*), \quad \rho^* = \rho(t,r^*). \tag{80}$$

The distribution of the neutron production function, $N_r(r)$, in Fig. 15 shows that the zone $r<5$ nm does not produce many neutrons and thus this zone does not need to be considered carefully. This is fortunate since it would require grids smaller than 0.1 nm, which differ computationally and put into question the continuum assumption for the model.

It is interesting that the maximum particle velocity near the bubble's center ($r\approx r^*=20-30$ nm) reaches $w^* \approx 600-800$ km/s, but this state takes place during only $\Delta t^* \sim 0.05-0.1$ ps, so that the displacement of the plasma particles, $w^*\Delta t^* \sim 30$ nm, is very small. Indeed, it looks almost like an "infinite speed ($w^*=\infty$) during a zero time interval ($\Delta t^*=0$)."

Mathematically the kinetics (61)–(63) of the cumulative neutron emission, N, is a numerical convolution of the singularity at $r=0$ at the moment, t^∞, during reflection of the shock wave from the center ($t_{23}<t^\infty<t_{24}=t_{23}+0.01$ ps, see Fig. 13), when the temperature is near infinite at the center ($r=0$). This convolution makes it possible to calculate numerically by finite difference equations the neutron emission in spite of the almost infinite temperature spike at the bubble's center.

Besides the initial moment of the time [$t=0$, see (74)–(76)], when the growth of the microbubbles was initiated, two other moments of the time are important. The first was the moment t°, when the bubble reaches its minimum radius ($a=a_{\min}$), and the time relative to this moment ($t-t^\circ$, $t^\circ \approx 41.993$ μs) was used in Figs. 10 and 11. The second moment was time t^*, when the temperature at the radius of the maximum neutron (and tritium) production ($r=r^*$) reaches its maximum value ($T^*=T^*_{\max}$), and the time relative to this moment ($t-t^*, t^* \approx t^\circ - 0.782$ μs) in picosecond and subpicosecond intervals was used in Figs. 12, 13, 16, and 17.

In Fig. 16 the evolutions of density ρ^*, pressure p^*, and temperature T^* are shown. It is seen that the evolution of the density of the gas in the central core takes place during five stages. The first stage ($t\approx 0-27$ μs) is a homobaric relatively slow expansion (see Figs. 7 and 14) when ρ_G falls from $\rho_0=0.25$ kg/m^3 to $\rho_{\min}=0.13$ kg/m^3. The second stage ($t\approx 27-41.9$ μs) is a relatively slow continuously accelerating compression when ρ_G grows from $\rho_{\min}=0.13$ kg/m^3 to $\rho_{\text{ad}}=4.8$ kg/m^3. This stage is practically isentropic (i.e., adiabatic). The third stage is the compression due to the leading shock wave (labeled by Sh in Fig. 16 where the density increases: $\rho_{\text{Sh}}/\rho_{\text{ad}}=(\rho_+/\rho_-)_{\max}=17$. The fourth stage is compression: $\rho^{(4)}/\rho_{\text{Sh}} \approx 5.9$ due to a continuous (during 0.2 ps) compression wave after the leading shock wave. This is similar to the Guderley solution.[81,82] The fifth stage is a large compression $\rho_{\max}/\rho^{(4)} \approx 24$ due to the interaction of the reflected leading shock wave from the center with a following continuous compression wave in the monatomic plasma. This stage is of very short duration, $\Delta t^{(5)} \sim 0.05$ ps, but it is not a compression by a single shock wave because the maximum compression of a monatomic gas ($\gamma=5/3$) due to a shock wave is only $(\rho_+/\rho_-)_{\max}=4$. The fifth stage occurs at $r=r^*$ about 0.2 ps later than the fourth stage. For no ionization this time is 0.7 ps. During all five stages the compression of the gas in the central core is very large, $\rho_{\max}/\rho_{\min} \approx 0.77\times 10^5$.

The third, fourth, and fifth stages are characterized by sharp changes of the time and spatial scales (i.e., blowup, or "sharpening").

The thermonuclear core consists of ions of carbon, deuterium, and oxygen. The ratio of the carbon, deuterium, and oxygen ions corresponds to their ratio in the acetone molecule C_3DO_6 (i.e., 3:6:1). The total number of the ions, N_i, in the highly compressed thermonuclear core is

$$N_i \approx \tfrac{4}{3}\pi r_c^3 \rho^* Z_i \mathrm{N}^{(A)}/M \sim 10^9$$
$$(\rho^* = 10 \text{ g/cm}^3,\ r_c = 60 \text{ nm},\ Z_i = 10,\ M = 64). \tag{81}$$

This equation implies that the interion or internuclear distance in the core is $l_i \sim 10^{-3} r_c$, and thus a continuum fluid dynamics approximation should be applicable for this region. However, our estimation of the ion's mean free path for the core (Appendix E) is $l_{\text{fp}} \sim 10^{-9}$ m, and thus the Knudsen number is $\mathrm{Kn}=l_{\text{fp}}/r_c \sim 10^{-2}$, which is near the limit for a continuum approximation of the thermal conductivity and shock waves (Appendix E) in the core region. Nevertheless, for the case being analyzed herein (i.e., the ORNL data[1,2]), it appears that the highly compressed core region can be accurately analyzed using a continuum approximation.

The evolution of the cumulative D/D neutron and tritium production function, $N(t)$ [see (64)], is shown during a subpicosecond time interval in Fig. 17. It is seen that D/D thermonuclear fusion takes place during a time interval of about 0.5 ps. The total number of emitted D/D neutrons, N, can be found from (63) using spatial integration of function N_r. For the sinusoidal incident pressure evolution with $\Delta p_1=15$ bars and $\Delta p_2=50$ bars this procedure gives $N \approx 3$ neutrons/bubble/implosion when there is ionization and $N \approx 3.7$ neutron/(bubble $\times$ implosion) if there is no ionization. A more realistic evaluation of the liquid pressure in the interior of the bubble cluster (see Fig. 6) yields (see Fig. 17)

$$N = 12 \text{ neutron/(bubble} \times \text{implosion)}. \tag{82}$$

The number of D/D thermonuclear neutrons produced may be checked qualitatively by estimating the integral in (63) using the mean value theorem:

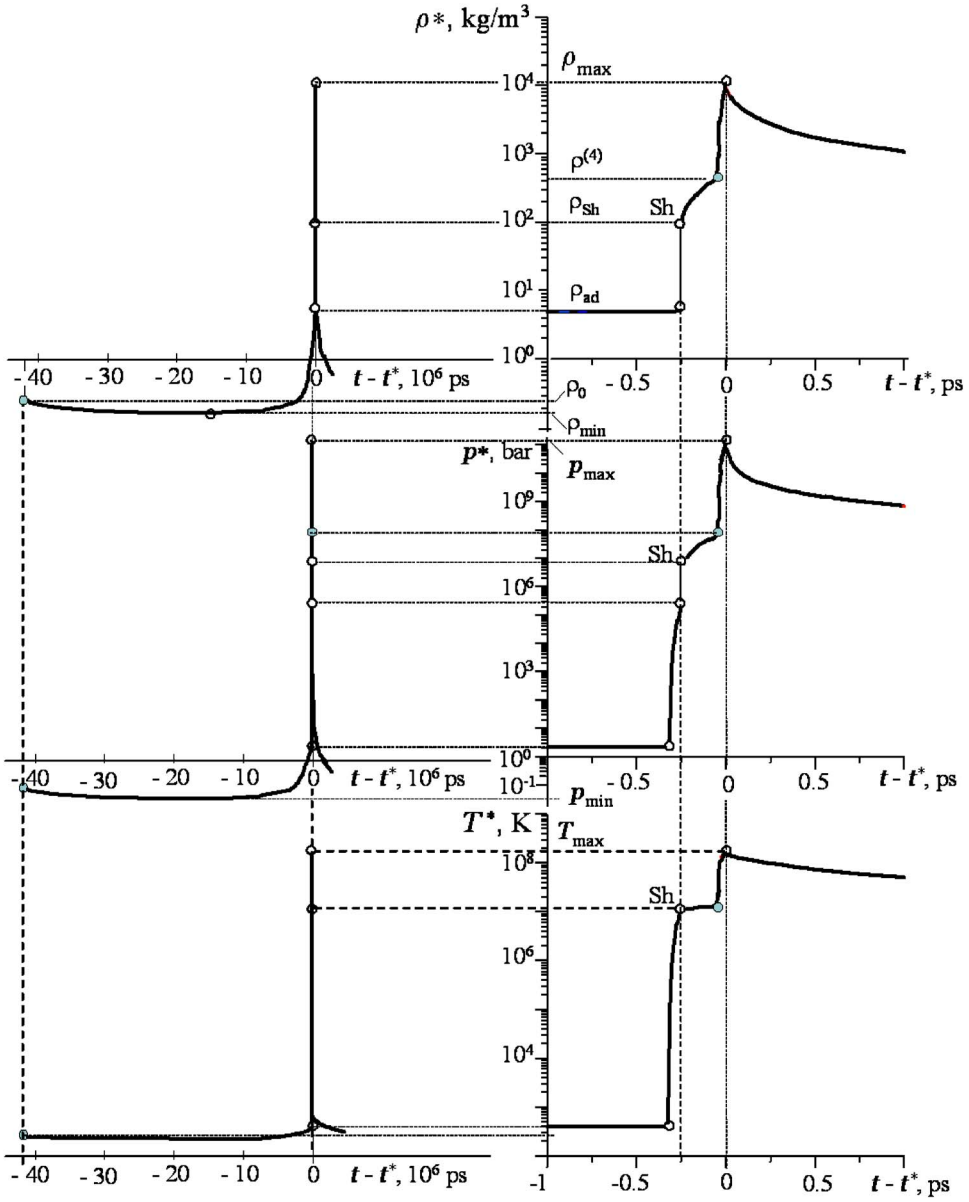

FIG. 16. Temporal distributions of density, pressure and temperature of the vapor corresponding to the radial location of maximum neutron production ($r=r^*$) during the subpicosecond, high Mach number, stage. The thick line is for an ionized vapor and the thin line is for a nonionized vapor.

$$N \sim (n_{D^*})^2 \langle \sigma v \rangle_* (r_*)^3 (\Delta t_*), \tag{83}$$

where r_* is the radius of the super compressed, ultrahot central core region of the bubble; Δt_* is the fusion reaction time; n_{D^*} is a characteristic concentration of deuterium ions in the central core region of the bubble, and $\langle \sigma v \rangle_*$ is the weighted nuclear cross section (Fig. 5). The ranges of these characteristic values are

$$n_{D^*} \approx 0.5 \times 10^{30}\ \mathrm{D/m^3}\ [\text{see (62) for } \rho_* \approx\ 10^4\ \mathrm{kg/m^3}],$$

$$\langle \sigma v \rangle_* \sim (3-7) \times 10^{-25}\ \mathrm{m^3/s}\ (\text{see Fig. 5 for } T_* \approx 10^8\ \mathrm{K}), \tag{84}$$

$$r_* \approx 50 \times 10^{-9}\ \mathrm{m}, \quad \Delta t_* \approx 0.5 \times 10^{-12}\ \mathrm{s}.$$

Equations (83) and (84) yield $N \sim 1-10$ neutrons/(bubble $\times$ implosion), which is quite consistent with the HYDRO code results, (82).

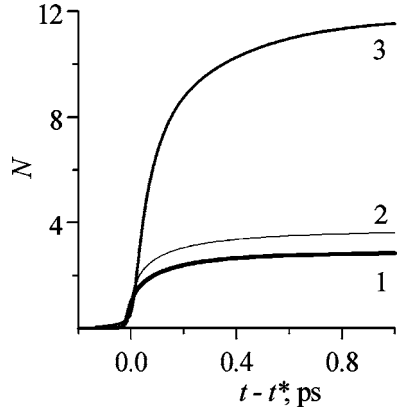

FIG. 17. The cumulative number of emitted D/D neutrons, $N(t)$; numerical labels (1) and (2) correspond to the results presented in Figs. 7–15, for $\Delta p_2 = 50$ bar, with ionization (1) and without ionization (2); (3) corresponds to the case with bubble cluster dynamics with the pressure intensification given in Fig. 6. All regimes correspond to a pool temperature of $T_{L0} = 273$ K and an accommodation coefficient of $\alpha = 0.2-1.0$.

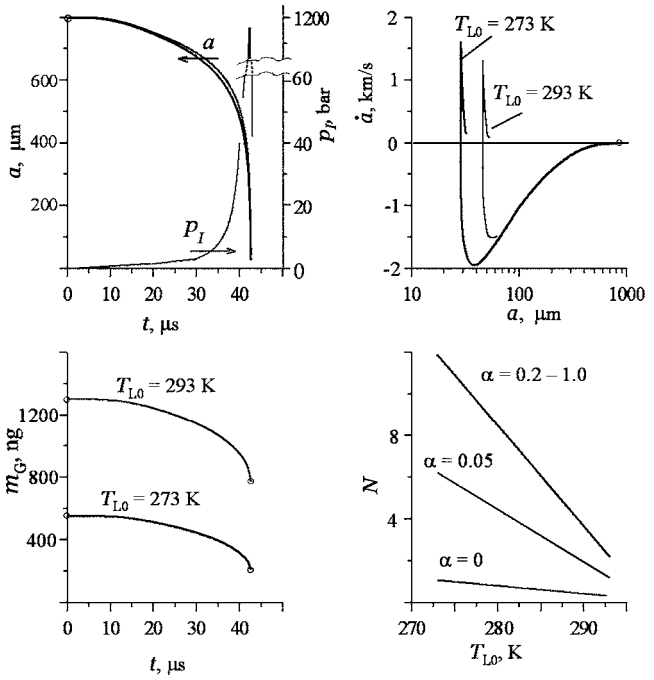

FIG. 18. Influence of the pool temperature (T_{L0}=273–293 K) and accommodation coefficient (α=0,0.05–1.0) on the evolution of bubble vapor mass (m_G), interfacial velocity ($\dot{a}$), and cumulative neutron production (N). The cluster dynamics with the amplified incident pressure shown in Fig. 6 was used in these calculations (see Fig. 6). The numerical labels correspond to various values of T_{L0} and α.

Finally, as can be seen in Fig. 18, the calculations show that increasing the liquid temperature from T_{L0}=273 K to T_0=293 K, or the use of a small accommodation (i.e., condensation) coefficient, α, significantly decreases the number of D/D thermonuclear neutrons produced [e.g., $N \approx 1$ neutron/(bubble×implosion) for T_{L0}=293 K, $\alpha \sim 0.05$], which corresponds to our experimental findings.[1,2] This seeming paradox for liquid pool temperature can be easily explained. For higher pool temperatures the saturation pressure is higher [$p_S(293\ \mathrm{K}) \approx 3.5\ p_S(273\ \mathrm{K})$], thus the mass of the vapor generated during bubble expansion at T_0 =293 K is larger than at 273 K. Also, vapor condensation is reduced since the liquid pool is not as cold. As a result the pressure of the vapor during the compression of the bubble becomes higher than for a cooler liquid pool and the final interface velocity, $w_{La} \approx \mathrm{d}a/\mathrm{d}t$, which creates the compression wave that moves toward the bubble's center, is slower. In addition, for higher temperatures of the liquid pool the frequency of new bubble cluster formation, f_{CL} [see the discussion before (1)], may decrease because of the slower disappearance of the previous bubble cluster due to rectified condensation in the warmer liquid.

Investigation of the pressure evolution in the bubble cluster (Sec. IX), given the external acoustic pressure field, (74), shows that the rarefaction in the cluster is smaller than −15 bars, but during the compression phase local liquid pressure inside the bubble cluster is much higher and shorter in duration than the external acoustic pressure (see Fig. 6). During rarefaction the maximum bubble radius within the bubble cluster reaches only 100–300 μm, which is too small to generate thermonuclear conditions in the imploded bubbles. However, as discussed in Sec. X, during the growth phase about 10–20 bubbles may coalesce forming relatively large bubbles of radius 600–800 μm. This size bubble provides sufficient focusing of the compression wave, and produces the thermonuclear conditions in the central core of the bubbles shown in Fig. 13. For 1000 bubbles in the initial bubble cluster,[1,2] after coalescence there would be 50–100 larger bubbles. Those in the central region of the cluster will be impacted by the local compression pressure, which is much higher than on the periphery of the bubble cluster (see Fig. 6), and the resultant implosion gives rise to the D/D neutron yield shown in Fig. 17.

As noted previously, the average amount of emitted neutrons from a single collapsing D-acetone vapor bubble in a chilled liquid pool (T_0=273 K) is about 12 neutrons per acoustic cycle for ORNL experimental conditions.[1,2] According to the experiment data of Taleyarkhan *et al.*[2] and our evaluations, (1), implosions of bubble clusters took place $f \approx 2100-2500$ times per second. If we assume that a bubble cluster contains $k \approx 15-20$ strongly collapsing bubbles, each of which produce $N \approx 12$ neutrons per implosion, we can estimate the number of emitted D/D neutrons per second:

$$P \approx kfN \approx (5 \pm 1) \times 10^5\ \mathrm{n/s}, \tag{85}$$

which is in good agreement with the experimental value;[1,2] see (1). In any event, it is clear that the predicted conditions within imploding bubbles are suitable for D/D thermonuclear fusion, and it appears that scale-up of the neutron yield may be possible.[5]

XII. CONCLUSIONS

Our theoretical and numerical analyses have shown that the acoustically forced implosion of vapor bubbles of radius $a_{\max} \sim 600-800$ μm in a bubble cluster due to a 15 bar incident pressure around the cluster and pressure amplification within the cluster, is accompanied by the formation of a strong compression shock wave cumulating (focusing) toward the center of the bubbles. This shock wave reflects from the center of the bubble producing extremely high local velocities ($w_* \approx 1000$ km/s), and a hot ($T_* \approx 2 \times 10^8$ K), dense ($\rho_* \approx 10$ g/cm^3), high pressure ($p_* \approx 10^{11}$ bars) plasma core of radius $r \leqslant 60-65$ nm, having $\sim 10^9$ nuclei. This extreme state lasts for only a very short time ($\Delta t_* \approx 10^{-13}-10^{-12}$ s). If this core is comprised of a deuterated hydrocarbon vapor (e.g., D-acetone) during this state, thermonuclear D/D fusion can take place producing about 12 fast neutrons (2.45 MeV) per bubble per implosion, and an equivalent amount of tritium. In any event, our analysis strongly supports the plausibility of the experimental results on bubble fusion[1,2] and the prior speculations about sonofusion of other researchers.[33]

Some important features of the bubble fusion process are as follows:

(1) *The cold liquid effect*—where relatively small variations of the liquid pool temperature strongly influence the kinetic energy of the liquid and thus the intensity of the thermonuclear fusion reaction.

(2) *The bubble cluster effect*—where bubble cluster dynamics produces a significant amplification of the interior liquid pressure compared with the incident pressure of the impressed acoustic field.
(3) *The bubble coalescence effect*—which promotes the formation of larger bubbles within the bubble cluster, having a maximum radius of $a_{\max}=600-800$ μm. This allows for a high cumulation of the shock waves near the center of the bubble producing conditions in a central core region of the imploded bubbles which are suitable for thermonuclear fusion.
(4) *Nondissociation of the liquid*—where, in spite of the high pressures experienced (10^5-10^6 bars), the liquid near the interface has insufficient time for dissociation (10 ns). This is why the liquid is much less compressible than implied by an equilibrium adiabat, which corresponds to more than a microsecond of compression. Thus extrapolation of first part of D-U shock adiabat should be used for the estimation of compressibility of the liquid. This implies stronger shock waves in the bubble since less strain energy is built up in the liquid.
(5) *"Cold" electrons*—where during the extremely short time of the ultrahigh compression process ($10^{-13}-10^{-12}$ s), the electrons have little time to be heated by the ions and the electron temperatures are many times less than ion temperatures $T_e \ll T_i$ [see discussions associated with (58)]. Thus the heat capacity of the vapor is $\sim$2000 J/kg instead of the equilibrium heat capacity of completely ionized plasma, $\sim$8000 J/kg. This causes the temperature of the ions to be about four times higher than for equilibrium plasma, which, in turn, results in conditions suitable for thermonuclear fusion. Moreover, the "cold" electrons do not produce significant energy losses by radiation emissions.
(6) *Multiscale phenomena*—where the energetic collapse of the bubbles is a multiscale phenomenon with a final rapid change of the scale (blowup, or "sharpening"), and during the different stages, different physical phenomena, spatial and time scales dominate the process. These physical processes are heat transfer, evaporation, condensation, and transition from a two-phase mixture to a supercritical fluid. The transition from an incompressible liquid and a homobaric pressure distribution in the vapor (this stage occupies most of the time of the process (i.e., 41.5 μs from 42 μs) to high compression of the liquid and to shock wave phenomena in gas (0.5 μs in duration), dissociation, ionization, and finally to thermonuclear fusion conditions. The spatial scales are the following: the acoustic field scale is $R_{\mathrm{AC}}\sim 10^{-2}$ m, the bubble cluster scale is $R\sim 10^{-3}$ m, the bubble size scale is $a\sim 10^{-5}-10^{-4}$ m, the dissociated core size scale is $\sim 10^{-6}$ m, the ionized core scale is 10^{-7} m, and the thermonuclear core scale is $10^{-8}-10^{-7}$ m. The time scales are the following: the evaporation and condensation time scale is $\sim 10^{-5}$ s, the compression wave time scale is $\sim 10^{-6}$ s, the dissociation time scale is $\sim 10^{-9}$ s, the time scale for full ionization is $10^{-11}-10^{-10}$ s, and the thermonuclear reaction time scale is 10^{-13} s. The numerical code must vary the equations to accommodate the different physical phenomena and use different size grids and different time steps (from $\Delta t=10^{-7}$ s to 10^{-14} s). To clarify the process, in the tiny central thermonuclear core this zone should use cell sizes of $\Delta r=10^{-10}$ m in a bubble of radius 10^{-5} m. The same problem exists for the thin boundary layers near the interface. The thermonuclear fusion process that occurs in imploding cavitation bubbles takes place within a spatial scale of about a few tens of nanometers and a time scale of a few tenths of a picosecond. Thus we might refer to it as a "nanopicosecond bubble fusion" process.
(7) *Three-dimensional phenomena*—where multidimensional analyses (which are presented in the separate papers[5,79,88]) of the shape of the bubble supports the assumption of a spherically symmetric flow (i.e., shock wave) creating the concentration of the energy in the interior of the imploding bubbles.

All these effects are crucial for the prediction of the thermonuclear reaction's intensity. In addition, to achieve nanoscale thermonuclear fusion it is important for the test liquid to have the following:

(1) A high atomic fraction of deuterium atoms in the molecule (in D-acetone it is 6/10=60%).
(2) A high molecular weight (i.e., a low sound speed in the vapor, which promotes a strong shock wave) and high condensation (accommodation) coefficient to mitigate vapor cushioning during bubble implosion (for D-acetone, $M=64$ and $\alpha \geqslant 0.2$).
(3) A low saturation pressure of vapor (which can be a property of the test fluid or can be achieved due to a low pool temperature).
(4) Weak nonlinear compressibility of the liquid.
(5) High cavitation strength of the liquid.

It is important to note that heavy water (D_2O) is not very appropriate for cavitation bubble fusion because of its relatively low molecular weight ($M=20$), high sound speed in vapor, low accommodation coefficient ($\alpha \approx 0.05-0.07$), relatively high nonlinear compressibility, and low cavitation strength.

It is also not appropriate to use laser-generated bubbles in bubble fusion experiments because these bubbles are relatively large and nonspherical, and have comparatively large vapor mass, which does not permit the liquid around an imploding bubble to reach a high kinetic energy because of cushioning by the uncondensed vapor. Moreover, lasers do not produce suitable bubble clusters,[5] which are essential to the achievement of thermonuclear conditions. These appear to be the main reasons that Geisler *et al.*[89] were not able to obtain D/D neutron emissions during laser-induced cavitation experiments in heavy water.

ACKNOWLEDGMENTS

This work is supported by the Russian Academy of Sciences, the Russian Foundation for Basic Research (Grants No. 05-01-00045 and No. 04-01-080050), and a research

grant from Oak Ridge National Laboratory (DARPA subcontract).

APPENDIX A: DISSOCIATION AND IONIZATION ENERGIES

The energy required for full dissociation of acetone was calculated in two steps. First, we note

$$C_3D_6O = 3C + \tfrac{1}{2}O_2 + 3D_2 + Q_m. \tag{A1}$$

Here Q_m is the specific (i.e., per mole of acetone) energy required for dissociation of a D-acetone (C_3D_6O) molecule into three atoms of carbon, C, one half a molecule of oxygen, O_2, and three molecules of deuterium, D_2. The second step is

$$O_2 = [(O + O) + Q_{O2}], \quad D_2 = [(D + D) + Q_{D2}]. \tag{A2}$$

Here Q_{O2} is the energy of dissociation of molecular oxygen (per mole of the oxygen, O_2) into two atoms of oxygen (O); Q_{D2} is the energy for dissociation of molecular deuterium, D_2 (per mole of the deuterium, D_2) into two atoms of D. These dissociation energies are given by (Gordon and Ford[72])

$$Q_m = 223 \times 10^6 \text{ J/kmol}, \quad Q_{O2} = 498 \times 10^6 \text{ J/kmol}, \quad Q_{D2} = 444 \times 10^6 \text{ J/kmol}. \tag{A3}$$

As a result the latent energy required for full dissociation per unit mass of D-acetone into the respective atoms is

$$\varepsilon_d^{(ch)} = \tfrac{1}{64}\left[Q_m + \tfrac{1}{2}Q_{O2} + 3Q_{D2}\right] = 28.2 \times 10^6 \text{ J/kg}. \tag{A4}$$

The energies of ionization for the electrons noted in (22) are given by (Gordon and Ford[90])

$$T_{D1} = 13.60 \text{ eV}, \quad T_{C4} = 64.49 \text{ eV}, \quad T_{O2} = 35.19 \text{ eV}, \quad T_{O6} = 138.1 \text{ eV},$$
$$T_{C1} = 11.26 \text{ eV}, \quad T_{C5} = 392.0 \text{ eV}, \quad T_{O3} = 54.94 \text{ eV}, \quad T_{O7} = 793.3 \text{ eV},$$
$$T_{C2} = 23.38 \text{ eV}, \quad T_{C6} = 490.0 \text{ eV}, \quad T_{O4} = 77.41 \text{ eV}, \quad T_{O8} = 871.4 \text{ eV},$$
$$T_{C3} = 47.89 \text{ eV}, \quad T_{O1} = 13.69 \text{ eV}, \quad T_{O5} = 113.9 \text{ eV}.$$

APPENDIX B: COEFFICIENTS FOR THE "COLD" POTENTIAL AND GRUNEISEN COEFFICIENT

For the molecular (i.e., nondissociated) state of liquid ($k=L$) acetone (high density, $\rho/\rho_{L0} > 0.3$) and corresponding to the left saturation curve $\rho_{LS}(p)$ and to the straight line of the shock adiabat, labeled NDis in Fig. 2, and using (30a), the appropriate parameters for $\varepsilon_L^{(p)}(\rho)$ and $p_L^{(p)}(\rho)$ are

$$A_L = 0.097\,57 \times 10^9 \text{ Pa}, \quad b_L = 19.07,$$
$$\rho_0 = \rho_{L0} = 858 \text{ kg/m}^3, \tag{B1}$$
$$\beta_L = \tfrac{1}{3}, \; K_L = 0.4535 \times 10^9 \text{ Pa}, \quad E_L = 0, \quad \xi_L = 1.$$

The heat capacity of the liquid and the density for the liquid were the same as in (7a): $c_L = c_{L0} = 1517$ J/(kgK), $\rho_{L0} = 858$ kg/m^3. The coefficients determining the Gruneisen coefficient, $\Gamma(\rho)$ in (32) are

$$a^{(0)} = 0.8337, \quad a^{(1)} = -0.728, \quad a^{(2)} = 2.934, \tag{B2}$$
$$\rho^{(1)} = 0.857\rho_{L0}, \quad \rho^{(2)} = 1.440\rho_{L0}.$$

To improve the approximation (24) and (25) with coefficients (B1) for high-density liquid ($\rho \geqslant \rho_{L0}$), and conserve a good approximation for the left saturation curve $\rho_{LS}(p) < \rho_{L0}$, the following correction term was used:

$$\Delta p^{(p)}(\rho) = A'\left(\frac{\rho}{\rho_{L0}} - 1\right)^6,$$

$$\Delta\varepsilon^{(p)}(\rho) = \int_{\rho_{L0}}^{\rho} \frac{\Delta p^{(p)}(\rho)}{\rho^2} \quad (A' = 1.0 \times 10^{11} \text{ Pa}, \; \rho \geqslant \rho_{L0}), \tag{B3}$$

$$\Delta p^{(p)}(\rho) = 0, \quad \Delta\varepsilon^{(p)}(\rho) = 0 \quad (\rho < \rho_{L0}).$$

Then the characteristic values ρ_L° and ε_L°, satisfying the boundary condition (26) are

$$\rho_L^\circ/\rho_{L0} = 1.331, \quad \varepsilon_L^\circ = 0.5978 \times 10^6 \text{ J/kg}. \tag{B4}$$

The exponential terms in potential (24) and (25) are negligibly small for $\rho/\rho_{L0} < 0.6$; in particular, for the critical point ($\rho_{cr}/\rho_{L0} = 0.360$). That is why for molecular (nondissociated) vapor in the near critical region one can use the Lennard-Jones potential which has only four correlation parameters, $E_m, K_m, \alpha_m, \xi_m$, and these parameters can be calculated independently of the exponential term with A and b using the conditions at the critical point [see (37)]. Then we have three equations for four parameters

$$E'_m - K'_m + \Gamma_m \rho_{cr} c_m T_{cr} = p_{cr},$$
$$(\alpha_m + 1)E'_m - (\xi_m + 1)K'_m + \Gamma_m c_m T_{cr} = 0,$$
$$\alpha_m(\alpha_m + 1)E'_m - \xi_m(\xi_m + 1)K'_m = 0,$$
$$E'_m = E_m\left(\frac{\rho_{cr}}{\rho_{L0}}\right)^{\alpha+1}, \quad K'_m = K_m\left(\frac{\rho_{cr}}{\rho_{L0}}\right)^{\xi+1}. \tag{B5}$$

The fourth necessary condition for these parameters is to have a good correlation with the right hand saturation curve

where $\rho_{GS}(p) \leqslant \rho_{cr}$. The parameters of the exponential term (A and b) were calculated to have good agreement with the shock adiabat $p(\rho)$ [see (31)] corresponding to the experimental shock adiabat (30a) for the nondissociated liquid after the shock wave. Thus all coefficients for nondissociated acetone vapor ($k=m$) are

$$A_m = 0.040 \times 10^9 \text{ Pa}, \quad \rho_0 = \rho_{L0} = 858 \text{ kg/m}^3,$$

$$b_m = 24.028, \quad \beta_L = \tfrac{1}{3}, \quad K_m = 1.784 \times 10^9 \text{ Pa}, \tag{B6}$$

$$E_m = 1.7435 \times 10^9 \text{ Pa}, \quad \alpha_m = 0.9394, \quad \xi_m = 0.900,$$

and using term (A3) for $\Delta p^{(p)}(\rho)$ and $\Delta \varepsilon^{(p)}(\rho)$. The parameters ρ_m° and ε_m°, ensuring the boundary condition (23), and the constant chemical component $\varepsilon_m^{(ch)}$ in (20) are

$$\rho_m^\circ/\rho_{L0} = 1.0016, \quad \varepsilon_m^\circ = 0.1503 \times 10^6 \text{ m}^2/\text{s}^2,$$
$$\varepsilon_m^{(ch)} = 0.5399 \times 10^6 \text{ J/kg}. \tag{B7}$$

For all states of acetone liquid ($k=L$) and gas ($k=1,2,\ldots, Z$) the potential terms for $p^{(p)}(\rho)$ and $\varepsilon^{(p)}(\rho)$ are essential only for high densities ($\rho/\rho_{L0} > 0.1$) because for low densities and high temperatures ($T > 10^3$ K),

$$p^{(p)} \ll p^{(T)}. \tag{B8}$$

That is why the coefficients of the elastic potential for the dissociated and ionized states may be calculated using the straight line shock wave adiabat corresponding only for dense ($\rho/\rho_{L0} > 1$) dissociated substances [see (27)] marked by the label "Dis" in Fig. 2. For the dissociated gas state ($k=d$) irrespectively of the levels of ionization x_k ($k=1, 2, \ldots, 14$) the appropriate coefficients for elastic terms are

$$A_d = 6.500 \times 10^9 \text{ Pa}, \quad \rho_0 = 2000 \text{ kg/m}^3, \quad b_d = 16.00,$$
$$E_d = 0, \quad K_d = 0.500 \times 10^9 \text{ Pa}, \quad \xi_d = \tfrac{1}{3}, \quad \beta_d = \tfrac{4}{3}. \tag{B9}$$

And the correction terms for very high densities ($\rho > 10\,000$ kg/m^3) are

$$\Delta p^{(p)}(\rho) = A'\left(\frac{\rho}{\rho_*} - 1\right)^3$$

$$(A' = 1.0 \times 10^{16} \text{ Pa}, \ \rho_* = 10\,000 \text{ kg/m}^3),$$

$$\Delta \varepsilon^{(p)}(\rho) = \int_{\rho_*}^{\rho} \frac{\Delta p^{(p)}(\rho)}{\rho^2}.$$

The parameters satisfying the boundary condition (26) are

$$\rho_d^\circ/\rho_{L0} = 2.068, \quad \varepsilon_d^\circ = 0.7111 \times 10^6 \text{ J/kg}. \tag{B10}$$

APPENDIX C: HOMOBARICITY OF GAS AND INCOMPRESSIBILITY OF LIQUID AT LOW MACH NUMBERS

Using the scales of ρ, w, p marked by subscript 0 (ρ_0, w_0, p_0), spatial and time scales (δ, τ), and using nondimensional variables:

$$\bar{\rho} = \frac{\rho}{\rho_0}, \quad \bar{w} = \frac{w}{w_0}, \quad \bar{p} = \frac{p}{p_0}, \quad \bar{r} = \frac{r}{\delta}, \quad \bar{t} = \frac{t}{\tau}, \tag{C1}$$

the fluid dynamic momentum conservation equation for spherically symmetrical flow may written as

$$\frac{\rho_0 w_0 \delta}{p_0 \tau}\frac{\partial \bar{w}}{\partial \bar{t}} + \frac{\rho_0 w_0^2}{p_0}\bar{w}\frac{\partial \bar{w}}{\partial \bar{r}} = \frac{\partial \bar{p}}{\partial \bar{r}}. \tag{C2}$$

The scales are chosen to make all nondimensional variables and their derivatives be on the order of unity. For the low Mach stage ($\tau^{-1} \sim \omega$) we can chose the characteristic scales as: $\delta = a, w_0 = \delta/\tau$ (for the typical SL and bubble fusion experiments, $\delta \sim 10\text{–}100$ μm, $\tau \sim 10$ μs, $w_0 \sim 1\text{–}10$ m/s, $\bar{w} \sim 1$), and in this case $\partial \bar{w}/\partial \bar{t}$ and $\bar{w}\,\partial \bar{w}/\partial \bar{r}$ will be on the order of unity. Then the momentum conservation equation may be rewritten as

$$\Pi\left(\frac{\partial \bar{w}}{\partial \bar{t}} + \bar{w}\frac{\partial \bar{w}}{\partial \bar{r}}\right) = \frac{\partial \bar{p}}{\partial \bar{r}} \quad \left(\Pi = \frac{\rho_0 w_0^2}{p_0}\right). \tag{C3}$$

In the gas/vapor $\rho_0 = \rho_G$, and $p/\rho_G \sim C_G^2$ (C_G is speed of sound in vapor), and $\Pi \sim w^2/C_G^2 = \mathsf{M}^2$, where M is the Mach number in the gas. Thus for low Mach numbers, that is where $\mathsf{M} \equiv |w|/C_G < \mathsf{M}_* (\mathsf{M}_* \approx 0.05\text{–}0.2)$, a homobaric approximation ($\partial \bar{p}/\partial \bar{r} \ll 1$, i.e., quasistatic approximation without inertial forces) for the vapor inside the bubble is applicable.

It should be noted that for SBSL and bubble fusion experiments the high Mach number implosion stage is very short ($\tau \sim 0.1$ μs) and the characteristic spatial scale for velocity distribution in the bubble can be small ($\delta \ll a$), but the velocity scale, $w_0 \sim 10^3$ m/s, is comparable with the sound speed. Then the scale coefficients $(\rho_0 w_0 \delta/(p_0 \tau)$ and $(\rho_0 w_0^2/p_0)$ in (C2) and Π in (C3) become large. Thus for large Mach numbers the vapor pressure is no longer uniform (i.e., $\partial \bar{p}/\partial \bar{r} \sim 1$).

In the liquid $\rho_0 = \rho_L \gg \rho_G, \Pi \sim 1$, and pressure gradient is also important ($\partial \bar{p}/\partial \bar{r} \sim 1$) even for the low Mach number noncollapsing stage. However, compressibility of the liquid for this stage ($\Delta p \sim \rho_L w_0^2$) is determined by $\Delta \rho_L/\rho_L \approx \Delta p/(\rho_L C_L^2) \sim w_0^2/C_L^2 \sim \mathsf{M}_L^2$, where M_L is Mach number in the liquid. Thus for the low Mach number noncollapsing stage ($\mathsf{M}_L^2 \ll 1$) an incompressibility approximation ($\Delta \rho_L/\rho_L \ll 1$) for the surrounding liquid may be used.

These estimations were explicitly formulated and investigated by Nigmatulin[33] and by Nigmatulin and Khabeev.[34]

APPENDIX D: EVAPORATION AND CONDENSATION INTENSITY

The Hertz-Knudsen-Langmuir formula for the resulting phase-transition intensity (Volmer,[61] Schrage,[62] Nigmatulin[33]) defined it by the saturation pressure, p_S, and the parameters of the liquid and vapor on the interface is

$$j = \frac{\alpha}{\sqrt{2\pi(R/M)}}\left(\frac{p_S(T_{La})}{\sqrt{T_{La}}} - \frac{\chi_G p_{Ga}}{\sqrt{T_{Ga}}}\right), \tag{D1}$$

where χ_G is a correction factor that results from the net motion of the vapor towards the surface that is superimposed on

an assumed Maxwellian velocity distribution of the vapor molecules:

$$\chi_G = \exp(-\Omega^2) - \Omega\sqrt{\pi}\left(1 - \frac{2}{\sqrt{\pi}}\int_0^{\Omega} \exp(-x^2)\mathrm{d}x\right), \quad \text{(D2)}$$

where

$$\Omega = \frac{j}{\sqrt{2}p_{Ga}}\sqrt{\frac{R}{M}T_{Ga}} = \frac{\dot{a} - w_{Ga}}{\sqrt{2(R/M)T_{Ga}}}.$$

In general, the temperature on the interface undergoes a jump $[T]$:

$$T_{La} - T_{Ga} = [T]. \quad \text{(D3)}$$

Analysis of the transfer processes in a thin Knudsen layer of vapor (having a thickness of a few mean free paths) leads to Labuntsov's formula (Nigmatulin[33])

$$[T] = 0.45\frac{jT_S(p_{Ga})}{\rho_{Ga}\sqrt{2(R/M)T_S(p_{Ga})}}. \quad \text{(D4)}$$

In general, these equations do not provide an explicit formula for the phase change mass flux, j, and one should solve the nonlinear system of equations (D1)–(D4) at any time along with the integration of the whole problem. However, this is a computationally time-consuming procedure. To mitigate the time of calculations one may use some simplifications.

First of all, the calculations in the present study show that the value of the temperature jump does not strongly influence the solution of the problem, and one may take

$$T_{La} = T_{Ga} = T_a, \quad \text{(D5)}$$

where T_a denotes the temperature of the interface.

Second, the parameter Ω, which represents the ratio of the overall relative speed of the vapor, $w_{Ga} - \mathrm{d}a/\mathrm{d}t$, to a characteristic molecular velocity, $\sqrt{2(R/M)T_{Ga}}$, is normally quite small. So, instead of (D2), an approximation for $\Omega \ll 1$ can be used, yielding

$$\chi_G \approx 1 - \sqrt{\pi}\Omega. \quad \text{(D6)}$$

Substituting (D5) and (D6) into (D1) one obtains

$$j = \frac{\alpha}{\sqrt{2\pi(R/M)T_a}}[p_S(T_a) - p_{Ga}] + \frac{1}{2}\alpha j, \quad \text{(D7)}$$

which is easily transformed to (49).

A more detailed derivation for the effective accommodation coefficient, f, in (49), accounting for the temperature jump at the interface, is given by Kucherov and Rikenglaz.[63] Colussi, Weavers, and Hoffman[28] and Storey and Szeri[29] have previously discussed the importance of the accommodation coefficient on SBSL and MBSL. As noted previously herein, this parameter is also of importance in the analysis of bubble fusion.

APPENDIX E: THERMAL CONDUCTIVITY OF ELECTRONS

In general, an electron gas obeys Fermi-Dirac quantum statistics, which in the case of sufficiently high temperatures turns into classical Boltzmann statistics. This happens when the electron temperature is much higher than temperature of quantum degeneration,

$$T_e \gg T^{(1)} \equiv \frac{h^2}{4\pi^2 m_e k^{(B)}} n_e^{2/3}, \quad n_e = \frac{\rho \mathrm{N}^{(A)}}{M} Z_e. \quad \text{(E1)}$$

Here n_e is the number density of electrons and Z_e is the number of electrons per molecule. For acetone $Z_e = 32$ [see (2)], m_e is the mass of an electron, h and $k^{(B)}$ are Planck and Boltzmann constants, respectively.

In addition to the criterion that the electron gas is classical, there is also an important criterion that it is ideal (i.e., the average kinetic energy of an electron is much larger than the average energy of interaction of the electron with its neighbor):

$$T_e \gg T^{(2)} \equiv \frac{e^2 n_e^{1/3}}{k^{(B)}}. \quad \text{(E2)}$$

A similar criterion for a gas of ions is

$$T_i \gg T^{(3)} \equiv \frac{(z_i e)2n_i^{1/3}}{k^{(B)}}, \quad n_i = \frac{\rho \mathrm{N}^{(A)}}{M} Z_i, \quad \text{(E3)}$$

where n_i is number density of ions, Z_i is mean number of ions per molecule of the fluid (for the acetone C_3D_6O, $Z_i = 3+6+1=10$), z_i is the mean charge of the ions (for acetone $z_i = Z_e/Z_i = 3.2$).

Depending on the combination of the compression rate of matter and the energy exchange between the electrons and ions during bubble implosion the electron temperature and density may be above or below these critical temperatures: $T^{(1)}, T^{(2)}, T^{(3)}$.

For an electron gas which is classical and ideal, $T_e \gg (T^{(1)}, T^{(2)})$, the heat transfer rate due to electron-electron collisions may be determined by a relaxation time (Zeldovich and Raiser[44]):

$$\tau_{\mathrm{ee}} \sim \frac{m_e^{1/2}(k^{(B)}T_e)^{3/2}}{n_e e^4 \ln \Lambda_e}, \quad \Lambda_e = \frac{l_{\mathrm{De}}}{\delta_e},$$
$$l_{\mathrm{De}} = \sqrt{\frac{k^B T_e}{n_e e^2}}, \quad \delta_e = \frac{e^2}{k^{(B)}T_e}, \quad \text{(E4)}$$

where $\ln \Lambda_e$ is the so-called Coulomb logarithm, Λ_e characterizes the ratio of Debye length l_{De} (a distance where screening of the Coulomb field takes place in an electron gas) to the characteristic impact parameter of electron-electron collisions, δ_e.

The relaxation time of the equilibrium state of the ionic component of the plasma is (Zeldovich and Raiser[44])

$$\tau_{\mathrm{ii}} \sim \sqrt{\frac{m_i}{m_e}}\tau_{\mathrm{ee}} \gg \tau_{\mathrm{ee}}. \quad \text{(E5)}$$

The relaxation time of the equilibrium between the electrons and the ions is

$$\tau_{ei} \sim \frac{m_i}{m_e}\tau_{ee} \gg \tau_{ii} \gg \tau_{ee}. \tag{E6}$$

Hence, the transfer of energy between the electrons and ions and a corresponding equalization of the electron and ion temperatures is a much slower process than the approach of either the electrons or ions to equilibrium separately.

Equations (E4)–(E6) imply that for densities $\rho \sim 10^4$ kg/m^3 and $T > 10^7$ K, which are characteristic for the thermonuclear fusion processes, $\tau_{ei} > 10^{-11}$ s. This means that for extremely high temperatures process, having a duration of $\sim 10^{-12}$ s, such as during bubble fusion, one may use the approximation of cold electrons.

Thus, it is reasonable to model the plasma in an imploding bubble as a two-temperature, two-component fluid where the ionic and electronic components have quite different temperatures. In a converging shock wave the ion temperature goes up very fast; however, due to inherent delays in the energy exchange between the ions and electrons (i.e., equilibration of the ion and electron temperatures needs $\tau_{ei} > 10^{-11}$ s), the electrons stay relatively cold. Further into the implosion process we have a very rapid rise in the density as well. Thus, the relatively cold electron gas may lose its ideal and classical properties. Moreover, as densities become higher the Debye length decreases and the relaxation time τ_{ee} goes up even before the classical approximations fail, and the electron gas may be trapped in its quantum degenerate state.

This allows us to make an important approximation, which is not normally valid in laser-induced inertial confinement fusion analysis (Duderstadt and Moses[53]). In particular, during the final stage of bubble implosion the electron gas can be neglected in the model, because being "light" and "cold" the electrons carry almost no mass, momentum and energy.

Therefore, there is no need to consider the energy exchange between the ions and electrons and the thermal conductivity of the electron gas. The thermal conductivity of such plasma is due to the ions.

APPENDIX F: THERMAL CONDUCTIVITY OF IONS

In contrast to the electrons, the ions are very hot and may be easily modeled as a classic ideal gas of positively charged particles. Kinetic theory gives the following equation for the ion-ion thermal conductivity in the plasma (Zeldovich and Raiser[44]):

$$\lambda_{ii} = \frac{k^{(B)}}{2\sigma_{ii}}\left(\frac{8k^{(B)}T_i}{\pi m_i}\right)^{1/2},$$

$$\sigma_{ii} = \frac{2\pi}{9}\frac{z_i^4 e^4}{(k^{(B)}T_i)^2}\ln\Lambda_i, \quad \Lambda_i = \frac{l_{Di}}{\delta_i}, \tag{F1}$$

$$l_{Di} = \sqrt{\frac{k^{(B)}T_i}{n_i z_i^2 e^2}}, \quad \delta_i = \frac{2}{3}\frac{z_i^2 e^2}{k^{(B)}T_i}.$$

For the ion temperatures and pressures that occur in the very hot and dense ($T_i = 10^7$ to 10^8 K, $\rho \sim 10^4$ kg/m^3) central zone of the imploding bubble, the estimated ion-ion thermal conductivity is very high [$\lambda_{ii} = 10^3 - 10^5$ W/(m K)]. However, there are two reasons why the actual thermal conductivity must be much lower; the concept of the local equilibrium state is not completely valid, and a theory based on Boltzmann transport equation is needed.

First, one can see that following (F1) the ion-ion interaction cross section, σ_{ii}, decreases with temperature as T^{-2}. However, it can not become infinitesimally small. Eventually, there has to be a limit (σ_0) corresponding to the situation that the relative velocities of the colliding ions are so high that the Coulomb forces are not dominant any more and ions collide almost like "elastic balls." This limit, σ_0, does not depend on temperature and pressure, but depends on the geometric dimensions of ions and therefore is a function of the atomic number. Thus, the ion/ion cross section, σ, may be corrected qualitatively by the following:

$$\sigma = \sigma_{ii} \text{ (for } \sigma_{ii} > \sigma_0), \quad \sigma = \sigma_0 \text{ (for } \sigma_{ii} < \sigma_0), \tag{F2}$$

where σ_{ii} is calculated from (F1), and σ_0 is taken to be 10^{-19} m^2.

Second, the high pressures and temperatures exist in the central core in the bubble for only a very short time ($t_c \sim 1$ ps), that is why the classic ion/ion thermal conductivity concept (F1), together with the use of Fourier's law in (52), must be revised for the central zone. These concepts are strictly valid only in case of local thermodynamic equilibrium. If the kinetic theory breaks down because local thermodynamic equilibrium cannot be defined within the system, a more general theory is required, based on the Boltzmann transport equation.

Time and space scales responsible for local thermodynamic equilibrium, that need 15–20 collisions between the ions, are a relaxation length, $l_r \gg l_{fp}$, and relaxation time, $\tau_r \gg \tau_{fp}$, where l_{fp} and τ_{fp} are the mean free path and mean time between the ion collisions, respectively.

The radius of the hot core in the imploding bubble is $r_* \sim 10^2$ nm (see Sec. X), where the final convergence of the shock wave and thermonuclear process, which is undergone, is much larger than l_r. However, the temperature rise in the hot core in $\tau_* \sim 10^{-1}$ ps, which is faster than τ_r.

Thus the approximation of local thermodynamic equilibrium can be assumed over space, but not over time. In this case the Boltzmann transport equation leads to a so-called relaxation form of the heat conduction law (Tien *et al.*[91]), which for one-dimensional motion of the gas of ions is

$$\tau_{ii}\frac{\partial q}{\partial t} + q = -\lambda_{ii}\frac{\partial T_i}{\partial x}. \tag{F3}$$

Here τ_{ii} is a relaxation time due to ion-ion collisions. For our temperature and density range when the electron temperature is much lower than the ion temperature an estimation gives $\tau_{ii} \sim 10^{-1}$ ps. According to (F3), the heat flux, q, can be expressed as an integral over the history of the temperature gradient,

$$q = -\frac{\lambda_{ii}}{\tau_{ii}}\int_{-\infty}^{t} \exp\left(-\frac{t-t'}{\tau_{ii}}\right)\frac{\partial T_i}{\partial x}(x,t')\,dt'. \tag{F4}$$

For a single harmonic of the temperature gradient we have

$$q = \frac{\lambda_{ii}}{\sqrt{1+(\omega\tau_{ii})^2}}\left(\frac{\partial T_i}{\partial x}\right)_0 \sin(\omega t - \alpha), \quad \tan\alpha = \omega\tau_{ii}. \quad \text{(F5)}$$

This means that an effective thermal conductivity coefficient may be taken as

$$\tilde{\lambda}_{ii} \sim \frac{\lambda_{ii}}{\sqrt{1+(\omega\tau_{ii})^2}}. \quad \text{(F6)}$$

If one takes $\omega = 2\pi/\tau_*$, where τ_* is a characteristic time of the temperature growth, and it turns out that $\tau_* \sim \tau_{ii}$, then (F6) leads to the estimation that an effective ion thermal conductivity is about one order of magnitude less than the equilibrium ion thermal conductivity. This is another reason why the actual thermal conductivity must be lower than predicted by classic kinetic theory in (F1).

It should also be noted that the temperature growth is so fast that complete ionization has no time to occur completely, thus the mean ion charge, z_i, was taken to be unity.

APPENDIX G: RADIATIVE THERMAL EXCHANGE IN PLASMA

A hot plasma emits light by an energy cascade from the ions, to the electrons, and then to the photons. Compression work is done on atoms providing the conditions for ionization, which is an entrainment of electrons. That creates high ion temperatures, but relatively low electron temperatures, as discussed previously.

The physical mechanisms responsible for electron-photon coupling are free-free transitions (i.e., bremsstrahlung emission and absorption), bound-free transitions (i.e., photoelectric ionization and recombination), and bound-bound (i.e., discrete) transitions. The first two types of electron transitions are responsible for a broad band spectrum of radiation and the third one for a line spectrum. In order to model the electron-photon coupling only one parameter need be specified, that is a photon absorption coefficient, κ_v, which, in general, is a function of plasma density, radiation frequency and, what is of most importance for the present study, the electron temperature, T_e.

If the radiation mean free path is much smaller than bubble size the approximation of local thermodynamic equilibrium between radiation and matter is applicable. This is the so-called optically thick approximation. In this case, the radiation energy per unit volume, e_r, and pressure of thermal radiation, p_r, are the following (Zeldovich and Raiser[44]):

$$e_r = e_r^{(e)} = \frac{4\sigma T_e^4}{c}, \quad p_r = \frac{e_r}{3} = p_r^{(e)} = \frac{4\sigma T_e^4}{3c}, \quad \text{(G1)}$$

where σ is the Stefan-Boltzmann constant and c is the speed of light.

Estimations show that the energy of radiation and the radiation pressure become comparable with the internal energy and pressure of the matter, only when electron temperature is around 10^6 K and higher. Since the maximum electron temperatures, T_e, during bubble implosions are around 10^5, we can neglect the energy of radiation, and the high losses associated with energy absorption by the electron gas, the radiation pressure, and the so-called electron thermal conductivity. Such a simplification is also appropriate in the case of the so called optically thin approximation, when the radiation mean free path is comparable to, or much larger than, the bubble size or the region in the bubble where light is emitted. This is easy to understand because in this case the energy of radiation and the radiation pressure are essentially equal to zero, and the thermal energy emitted by the hot plasma (i.e., the integrated emission coefficient) is proportional to σT_e^4.

It has been shown (Moss *et al.*[22,23]) that the electron thermal conduction and the opacity (i.e., light absorption) of the plasma in a collapsing gas bubble are the mechanisms which are mainly responsible for the picosecond duration of single bubble sonoluminescence emissions. Theoretical predictions of the measured optical output, pulse widths, and spectra are out of the scope of the present study. Nevertheless, the above model of a partially ionized plasma with distinct but coupled ion and electron temperature fields, associated losses by plasma thermal conduction, an emission model for coupling the ionization energy to the radiation field, and a model for the opacity of the radiating matter, is generally suitable for bubble fusion predictions.

[1] R. P. Taleyarkhan, C. D. West, J. S. Cho, R. T. Lahey, Jr., R. I. Nigmatulin, and R. C. Block, "Evidence for nuclear emissions during acoustic cavitation," Science **295**, 1868 (2002).
[2] R. P. Taleyarkhan, C. D. West, J. S. Cho, R. T. Lahey, Jr., R. I. Nigmatulin, and R. C. Block, "Additional evidence of nuclear emissions during acoustic cavitation," Phys. Rev. E **69**, 036109 (2004).
[3] R. I. Nigmatulin, R. P. Taleyarkhan, and R. T. Lahey, Jr., "The evidence of thermonuclear fusion D+D during acoustic cavitation," Vestnik ANRB (Ufa, Bashkortostan, Russia) **4**, 3 (2002).
[4] R. I. Nigmatulin, R. P. Taleyarkhan, and R. T. Lahey, Jr., "The evidence for nuclear emissions during acoustic cavitation revisited," Int. J. Power Energy Syst. **218-A**, 345 (2004).
[5] R. T. Lahey, R. Taleyarkhan, R. I. Nigmatulin, and I. Sh Akhatov, "Sonoluminescence and the search for sonofusion," Adv. Heat Transfer (in press).
[6] C. D. West and R. Howlet, "Timing of sonoluminescence flashes," Nature **215**, 727 (1967).
[7] B. P. Barber, R. Hiller, K. Arisaka, H. Fetterman, and S. Putterman, "Resolving the picosecond characteristics of synchronous sonoluminescence," J. Acoust. Soc. Am. **91**, 3061 (1992).
[8] J. Tian, J. A. Ketering, and R. E. Apfel, "Direct observation of microbubble oscillations," J. Acoust. Soc. Am. **100**, 3976 (1996).
[9] L. Crum and T. Matula, "Shocking revelations," Science **276**, 1348 (1997).
[10] R. Hiller, K. Weninger, S. Putterman, and B. P. Barber, "Effects of noble gas dopping in single-bubble sonoluminescence," Science **266**, 248 (1994).
[11] H. Metcalf, "That flashing sound," Science **279**, 1322 (1998).
[12] D. Lohse, "Lasers blow a bigger bubble," Nature **392**, 21 (1998).
[13] D. F. Gaitan, "Sonoluminescence and bubble stability," Phys. World **12**, 3 (1999).
[14] R. I. Nigmatulin, I. Sh. Akhatov, N. K. Vakhitova, and R. T. Lahey, Jr., "Hydrodynamics, acoustics and transport in sonoluminescence phenomena," in *Sonochemistry and Sonoluminescence*, edited by L. A. Crum, T. J. Mason, J. L. Reisse, and K. S. Suslick, NATO ASI Series (Kluwer, Boston, 1999).
[15] C. D. Ohl, T. Kurz, R. Geisler, O. Lindau, and W. Lauterborn, "Bubble dynamics, shock waves and sonoluminescence," Philos. Trans. R. Soc. London **357**, 269 (1999).
[16] W. B. McNamara, Y. T. Didenko, and K. S. Suslick, "Sonoluminescence temperatures during multi-bubble cavitation," Nature **401**, 772 (1999).

[17] G. Delgadino, F. Bonetto, and R. T. Lahey, Jr., "The relationship between the method of acoustic excitation and the stability of single bubble sonoluminescence of various noble gases," Chem. Eng. Commun. **189**, 786 (2002).
[18] F. J. Moraga, R. P. Taleyarkhan, R. T. Lahey, Jr., and F. J. Bonetto, "Role of very-high-frequency excitation in single-bubble sonoluminescence," Phys. Rev. E **62**, 2233 (2000).
[19] M. A. Margulis, "Sonoluminescence," Phys. Usp. **43**, 259 (2000).
[20] F. R. Young, *Sonoluminescence* (CRC, London, 2004).
[21] W. C. Moss, D. B. Clarke, J. W. White, and D. A. Young, "Hydrodynamic simulations of bubble collapse and picosecond sonoluminescence," Phys. Fluids **6**, 2979 (1994).
[22] W. C. Moss, D. B. Clarke, and D. A. Young, "Calculated pulse widths and spectra of a single sonoluminescing bubble," Science **276**, 1398 (1997).
[23] W. C. Moss, D. B. Clarke, J. W. White, and D. A. Young, "Sonoluminescence and the prospects for table-top micro-thermonuclear fusion," Phys. Lett. A **211**, 69 (1996).
[24] Some statements in Moss *et al.*'s papers (Refs. 21–23) are incorrect. In particular, the assumption of adiabatic gas behavior is incorrect. Actually, as shown in papers by Nigmatulin *et al.* (Ref. 14) and Vuong and Szeri (Ref. 25) during the entire expansion process, and for most of the compression process, the gas in the bubble is isothermal and its temperature is equal to the liquid pool temperature. It is easy to estimate that for times of about 30–50 μs (the typical period of bubble volume oscillations) in a bubble of radius about 50 μm, thermal perturbations in the gas have sufficient time to come into equilibrium with the surrounding liquid. Only during the final implosion stage, which has a time duration $\sim 10^{-9}$ s, when the bubble radius reduces from about 10 μm to its minimum, submicrometer size and gas velocities of about 10^3 m/s occurs, does adiabatic gas heating occur. However, this error does not change qualitatively the basic conclusions in Moss *et al.*'s papers.
[25] C. Camara, S. Putterman, and E. Kirilov, "Sonoluminescence from a single bubble driven at one megahertz," Phys. Rev. Lett. **92**, 124301 (2004).
[26] V. Q. Vuong and A. J. Szeri, "Sonoluminescence and diffusive transport," Phys. Fluids **8**, 2354 (1996).
[27] B. Gompf, R. Gunther, G. Nick, R. Pecha, and W. Eisenmenger, "Resolving sonoluminescence pulse width with time-correlated single photon counting," Phys. Rev. Lett. **79**, 1405 (1997).
[28] Due to the dynamics of a collapsing bubble cluster the pressure surrounding the interior central bubbles in the cluster during the implosion stage can be greatly intensified (Ref. 5). This effect is considered in Sec. IX and seen in Fig. 6.
[29] A. J. Colussi, L. K. Weavers, and M. R. Hoffman, "Chemical bubble dynamics and quantitative sonochemistry," J. Phys. Chem. **102**, 6925 (1998).
[30] B. D. Storey and A. J. Szeri, "Water vapour, sonoluminescence and sonochemistry," Proc. R. Soc. London **456**, 1685 (2000).
[31] Y. T. Didenko and K. S. Suslick, "The energy efficiency of formation of photons, radicals and ions during single-bubble cavitation," Nature **418**, 394 (2002).
[32] A. G. Lipson, V. A. Klyuev, B. V. Deryagin, Yu. P. Toporov, M. G. Sirotyuk, O. B. Khavroshkin, and D. M. Sakov, "Observation of neutrons from cavitation action on substances containing deuterium," Sov. Tech. Phys. Lett. **16**, 89 (1990) (in Russian).
[33] R. I. Nigmatulin, *Dynamics of Multiphase Media*, Vols. 1 and 2 (Hemisphere, New York, 1991).
[34] R. I Nigmatulin and N. S. Khabeev, "Dynamics of vapor-gas bubbles," Izv. Akad. Nauk SSSR, Mekh. Zhidk. Gaza **6**, 51 (1976) (in Russian).
[35] R. I. Nigmatulin, I. Sh. Akhatov, N. K. Vakhitova, and A. S. Topolnikov, "Bubble collapse and shock wave formation in sonoluminescence," in *Nonlinear Acoustics at the Turn of the Millennium, Proceedings of the 15th International Symposium on Nonlinear Acoustics, Gottingen, Germany, 1–4 September 1999*, edited by W. Lauterborn and T. Kurz (AIP, Melville, NY, 2000).
[36] A. Prosperetti, L. A. Crum, and K. W. Commander, "Nonlinear bubble dynamics," J. Acoust. Soc. Am. **83**, 502 (1988).
[37] A. G. Lipson, V. A. Kuznetsov, and G. H. Miley, "The D-D reaction yield in the course of dielectric breakdown of cavitation bubbles in dielectric deuterated liquids," Tech. Phys. Lett. **30**, 415 (2004).
[38] M. A. Margulis, *Sonochemistry and Cavitation* (Gordon & Breach, London, 1995).
[39] M. A. Margulis and I. M. Margulis, "Electrical effects on the pulsating surface of cavitation bubbles," Russ. J. Phys. Chem. **71**, 1706 (1997).
[40] In the paper of Lipson, Kuznetsov, and Miley (Ref. 37), which discusses the experiments of Taleyarkhan *et al.* (Refs. 1 and 2), it is supposed that during cavitation microbubble formation (i.e., the cohesion breaking of the continua liquid) in dielectric liquids, like acetone or water, the fresh interfaces are electrically charged. Based on the theory of Margulis (Ref. 38) and Margulis and Margulis (Ref. 39) the surface density charge is estimated as $10^{10}-10^{11}$ e/cm^2. Next it is supposed that the initial microbubble is filled with high-pressure vapor ($p\sim 10^3$ bars, $T\sim 10^3$ K), presumably because of the absorption of energy from the 14.1 MeV PNG neutrons that collide with the atoms of liquid. In that case the size of the high-pressure embryonic cavitation microbubbles is $a_0\sim 10$ nm and the vapor density equals the density of liquid. The high density of the vapor prevents an electrical discharge (i.e., spark) until after the expansion of the bubble (to $a_{\max}=0.3-1.0$ mm), where the vapor density becomes smaller and an electrical discharge (breakdown) takes place ionizing the deuterium atoms. Positively charged deuterons (deuterium nuclei) are then accelerated to the negatively charged interface. The authors (Ref. 37) do not mention very important details of calculations, in particular, the surface charge density evolution during expansion of the bubble when the interface increases by 10^9-10^{10} times as $(a_{\max}^2/a_0^2)$ and the surface density charge should decrease. Anyway, it is stated that the deuteron's kinetic energy reaches 4–9 keV. Lipson, Kuznetsov, and Miley (Ref. 37) suppose it is the collisions of these deuterons with the liquid at the negatively charged interface that produces thermonuclear fusion and light emission and they estimate the neutron production in very large interval as $P=10^2-10^7$ n/s. However, the intensity of thermonuclear neutron emission f was supposed by them to be equal to acoustic forcing frequency $f_{\mathrm{AC}}=20\times 10^3$ s^{-1}. Actually [see (1)] in the ORNL experiment (Refs. 1 and 2) it is much less: $f\approx 2300\pm 200$ s^{-1}. With the proper corrections these estimations give $P=10-10^6$ n/s. Anyway, even corrected these results do not compare well with the experiments of Taleyarkhan *et al.* (Refs. 1 and 2). That is almost all the D/D neutrons are produced not because of the cohesion breaking of the liquid (by acoustic-induced liquid tension and PNG neutron impact) but by the periodic acoustic pressure forcing of the bubbles in cluster over a number of acoustic periods [see derivation and discussion of (1)]. Also their theory implies light and neutron production when the radius of the bubble is near at its maximum; however, in the ORNL experiments it was found (Ref. 2) that correlated light and neutron emissions occurred when the bubbles imploded to about their minimum size when the temperatures densities and pressures are the highest. Finally their theory does not correlate with the observed pressure shock wave (see Sec. II) formed in the liquid and impacting the acoustic chamber's wall after each implosion [detected (Refs. 1 and 2) one acoustic transport delay (R_{AC}/C_L) after the neutron and SL light emissions].
[41] N. B. Vargaftik, *Reference Book on Heat Transfer and Physical Properties of Fluids* (Nauka, Moscow, 1972) (in Russian).
[42] C. F. Beaton and G. F. Hewitt, *Physical Property Data for the Design Engineers* (Hemisphere, New York, 1989).
[43] L. V. Altshuler, "Use of shock waves in high-pressure physics," Sov. Phys. Usp. **8**, 52 (1965).
[44] Y. B. Zeldovich and Y. P. Raizer, *Physics of Shock Waves and High-Temperature Hydrodynamic Phenomena* (Academic, New York, 1966).
[45] J. M. Walsh and M. H. Rice, "Dynamic compression of liquids from measurements on strong shock waves," J. Chem. Phys. **26**, 815 (1957).
[46] A. P. Babichev, N. A. Babushkina, and A. M. Bratkovsky, *Physical Quantities: Reference Book* (Energoatomizdat, Moscow, 1991) (in Russian).
[47] M. Born and J. E. Mayer, "Zur gittertheorie der ionenkristalle," Z. Phys. **75**, 1 (1932).
[48] V. N. Zharkov and V. A. Kalinin, *Equations of State of Solids at High Pressures and Temperatures* (Nauka, Moscow, 1968) (in Russian).
[49] S. J. Jacobs, "On the equation of state of compressed liquids and solids," NOLTR 68-214, United States Naval Ordnance Laboratory (White Oak, MD, 1968).
[50] M. Cowperthwaite and W. K. Zwisler, "The JCZ equations of state for detonation products and their incorporation into the TIGER code," in *Proceedings of the 6th International Symposium on Detonation*, ACR-221 (Office of Naval Research, Naval Surface Weapons Center, White Oak, MD, 1976), p. 162.
[51] L. D. Landau and E. M. Lifshitz, *Hydrodynamics* (Nauka, Moscow, 1988) (in Russian).
[52] Kh. A. Rakhmatulin, *Gas and Wave Dynamics* (Moscow University Press, Moscow, 1983) (in Russian).
[53] J. J. Duderstadt and G. A. Moses, *Interfacial Confinement Fusion* (Wiley, New York, 1981).

[54]R. F. Trunin, "Shock compressibility of condensed substances in strong shock waves of underground nuclear explosions," Phys. Usp. **37**, 1123 (1994).
[55]R. F. Trunin, M. V. Zhernokletov, N. F. Kuznetsov, O. A. Radchenko, N. V. Sichevskaya, and V. V. Shutov, "Compression of liquid organic substances in shock waves," Khim. Fiz. **11**, 424 (1992) (in Russian).
[56]H. Lin, B. D. Storey, and A. J. Szeri, "Inertially driven inhomogeneities in violently collapsing bubbles: The validity of the Rayleigh-Plesset equation," J. Fluid Mech. **452**, 145 (2002).
[57]H. Lamb, *Hydrodynamics*, 3rd ed. (Cambridge University Press, Cambridge, 1991).
[58]L. I. Sedov, *Mechanics of Continuous Media (World Scientific Series in Theoretical and Applied Mechanics, Vol. 4)* (World Scientific, Singapore, 1996).
[59]G. Batchelor, *An Introduction to Fluid Dynamics* (Cambridge University Press, Cambridge, 1970).
[60]R. I. Nigmatulin, I. Sh. Akhatov, N. K. Vakhitova, and R. T. Lahey, Jr., "On the forced oscillations of a small gas bubble in a spherical liquid-filled flask," J. Fluid Mech. **414**, 47 (2000).
[61]M. Volmer, *Kinetik der Phasenbildung* (Steinkopff, Dresden, 1939).
[62]R. W. Schrage, *A Theoretical Study of Interphase Mass Transfer* (Columbia University Press, New York, 1953).
[63]R. Ya. Kucherov and L. E. Rikenglaz, "The problem of measuring the condensation coefficient," Dokl. Akad. Nauk SSSR **133**, 1130 (1960) (in Russian).
[64]B. Paul, "Compilation of evaporation coefficients," J. Am. Rocket Soc. **32**, 1321 (1962).
[65]The equations of state in Sec. IV, together with the kinetic equations for dx_k/dt, make the thermodynamic model multiparametric when the internal energy, ε, is determined by $Z+3$ independent parameters $\rho, T, x_{d0}, x_1, x_2, \ldots, x_Z$. In contrast, in the papers of Moss *et al.* (Refs. 21–23) a quasiequilibrium model $[x_k = x_k(T)]$ was used. This model makes the equations of state two-parametric [i.e., $\varepsilon = \varepsilon(\rho, T), p = p(\rho, T)$]. However, the equations of state used by Moss *et al.* are thermodynamically incorrect because the Gibbs equation for the two parametric model of Moss *et al.* implies that the differential for entropy, s,

$$ds = \frac{1}{T}d\varepsilon - \frac{p}{T\rho^2}d\rho = \frac{1}{T}\left(\frac{\partial \varepsilon}{\partial T}\right)_\rho dT + \frac{1}{T}\left[\left(\frac{\partial \varepsilon}{\partial \rho}\right)_T - \frac{p}{\rho^2}\right]d\rho$$

is not a complete differential.
[66]R. A. Gross, *Fusion Energy* (Wiley, New York, 1984).
[67]H. S. Bosch and G. M. Hale, "Improved formulas for fusion cross-sections and thermal reactivities," Nucl. Fusion **32**, 611 (1992).
[68]I. Akhatov, O. Lindau, A. Topolnikov, R. Mettin, N. Vakhitova, and W. Lauterborn, "Collapse and rebound of a laser-induced cavitation bubble," Phys. Fluids **13**, 2805 (2001).
[69]E. Hairer, S. Norsett, and G. Wanner, *Solving Ordinary Differential Equations. I. Nostiff Problems*, 2nd ed., Springer Series in Computational Mathematics Vol. 8 (Springer, New York, 1993).
[70]S. K. Godunov, A. V. Zabrodin, M. Ya. Ivanov, A. N. Kraiko, and G. P. Prokopov, *Numerical Solution of Gas Dynamics Multidimensional Problems* (Nauka, Moscow, 1976) (in Russian).
[71]A. S. Topolnikov, "Numerical modeling of nonlinear oscillations of a gas bubble in liquid accounting for formation of shock waves," Ph.D. thesis, Bashkir State University, Ufa, Russia, December, 2000.
[72]Y.-C. Wang and C. E. Brennen, "Shock wave development in the collapse of a cloud of bubbles," Cavitation and Multiphase Flow, ASME **194**, 15 (1994).
[73]Y. Matsumoto, "Bubble and bubble cloud dynamics," in *Nonlinear Acoustics at the Turn of the Millennium, Proceedings of the 15th International Symposium on Nonlinear Acoustics, Gottingen, Germany, 1–4 September 1999*, edited by W. Lauterborn and T. Kurz (AIP, Melville, NY, 2000).
[74]M. Shimada, Y. Matsumoto, and T. Kobayashi, "Influence of the nuclei size distribution on the collapsing behavior of the cloud cavitation," JSME Int. J., Ser. B **43**, 380 (2000).
[75]V. K. Kedrinsky, *Hydrodynamics of Explosion. Experiment and Models* (SO RAN, Novosibirsk, 2000).
[76]R. I. Nigmatulin, V. Sh. Shagapov, I. K. Gimaltdinov, and M. N. Galimzyanov, "Two-dimensional pressure waves in liquid with bubbly zone," Phys. Dokl. **378**, 763 (2001).
[77]C. E. Brennen, *Cavitation and Bubble Dynamics* (Oxford University Press, New York, 1995).
[78]I. M. Margulis and M. A. Margulis, "Interaction dynamics of bubbles in a cavitation cloud," Russ. J. Phys. Chem. **78**, 1159 (2004).
[79]A. A. Aganin, R. I. Nigmatulin, M. A. Ilgamov, and I. Sh. Akhatov, "Dynamics of a gas bubble situated in the center of spherical liquid volume," Phys. Dokl. **44**, 734 (1999).
[80]A. J. Szeri, B. D. Storey, A. Pearson, and J. R. Blake, "Heat and mass transfer during the violent collapse of nonspherical bubbles," Phys. Fluids **15**, 2576 (2003).
[81]G. Guderley, "Starke kugelige und zylindrische verdichtungsstobe in der nahe des kugelmittelpunktes der zylinderachse," Luftfahrtforschung **19**, 302 (1942).
[82]F. L. Chernousko, "A converging shock-wave in a gas of variable density," J. Appl. Math. Mech. **24**, 1171 (1960).
[83]R. I. Nigmatulin, "Converging cylindrical and spherical detonation waves," J. Appl. Math. Mech. **31**, 171 (1967).
[84]E. I. Zababakhin and I. E. Zababakhin, *Unlimited Cumulation Phenomena* (Nauka, Moscow, 1990).
[85]H. Lin and A. J. Szeri, "Shock formation in the presence of entropy gradients," J. Fluid Mech. **431**, 161 (2001).
[86]V. A. Belokogne, "Effect of radiation amplitude of isothermal shock," Sov. Phys. Dokl. **202**, 1296 (1972).
[87]E. I. Zababakhin and V. A. Simonenko, "Spherical center compression wave," J. Appl. Math. Mech. **42**, 602 (1978).
[88]S. Nagrath, K. E. Jansen, R. T. Lahey, Jr., and I. S. Akhatov, "Hydrodynamic simulation of air bubble implosion using a FEM-based level set approach," J. Comput. Phys. (in press).
[89]R. Geisler, W. D. Schmidt-Ott, T. Kurz, and W. Lauterborn, "Search for neutron emission in laser-induced cavitation," Europhys. Lett. **66**, 435 (2004).
[90]A. Gordon and R. Ford, *The Chemist's Companion: Handbook of Reaction Data* (Wiley, New York, 1992).
[91]*Microscale Energy Transport*, edited by C. L. Tien, A. Majumdar, and F. M. Gerner (Taylor & Francis, Washington, DC, 1998).